International Journal of Nanomedicine

Dovepress
open access to scientific and medical research

Open Access Full Text Article

ORIGINAL RESEARCH

Doped Multiple Nanoparticles with Hydroxyapatite Coating Show Diverse Health Effects in vivo

Xinlin Li[1,2,*], Baojuan Yang[3,4,*], Mengfei Xu[1,2], Fangyi Li[3,4], Zhaoli Geng[1,2], Weiqiang Cui[3,4], Xingfu Sun[3,4], Yanle Li[3,4], Yi Liu[1,2]

[1]Department of Orthodontics, School and Hospital of Stomatology, Cheeloo College of Medicine, Shandong University, Jinan, Shandong, 250012, People's Republic of China; [2]Shandong Key Laboratory of Oral Tissue Regeneration, Shandong Engineering Laboratory for Dental Materials and Oral Tissue Regeneration, Shandong Provincial Clinical Research Center for Oral Diseases, Jinan, Shandong, 250012, People's Republic of China; [3]Key Laboratory of High Efficiency and Clean Mechanical Manufacture, Ministry of Education, School of Mechanical Engineering, Shandong University, Jinan, 250061, People's Republic of China; [4]National Demonstration Center for Experimental Mechanical Engineering Education, Shandong University, Jinan, 250061, People's Republic of China

*These authors contributed equally to this work

Correspondence: Yi Liu, Department of Orthodontics, School and Hospital of Stomatology, Cheeloo College of Medicine, Shandong University, No. 44-1 Wenhua Road West, Jinan, Shandong, 250012, People's Republic of China, Tel +86-531-88381630, Email yiliu@sdu.edu.cn; Yanle Li, Key Laboratory of High Efficiency and Clean Mechanical Manufacture, Ministry of Education, Shandong University School of Mechanical Engineering, No. 17923, Jingshi Road, Jinan, 250061, People's Republic of China, Tel +86-531-88392208, Email yanle.li@sdu.edu.cn

Introduction: The lack of osteoinductive, angiogenic and antimicrobial properties of hydroxyapatite coatings (HA) on titanium surfaces severely limits their use in orthopedic and dental implants. Therefore, we doped SiO_2, Gd_2O_3 and CeO_2 nanoparticles into HA to fabricate a HASiGdCe coating with a combination of decent antibacterial, angiogenic and osteogenic properties by the plasma spraying technique.

Methods: The HASiGdCe coating was analyzed by SEM (EDS), surface roughness tests, contact angle tests, XRD, FTIR spectroscopy, tensile tests and electrochemical dynamic polarization tests. Methicillin-resistant *Staphylococcus aureus* (MRSA) and *Pseudomonas aeruginosa* (PAO-1) were used as representative bacteria to verify the antibacterial properties of the HASiGdCe coating. We evaluated the cytocompatibility and in vitro osteoinductivity of the HASiGdCe coating by investigating its effect on the cell viability and osteogenic differentiation of MC3T3-E1 cells. We assessed the in vitro angiogenic activity of the HASiGdCe coating by migration assay, tube formation assay, and RT–PCR analysis of angiogenic genes in HUVECs. Finally, we used infected animal femur models to investigate the biosafety, antimicrobial and osteointegration properties of the HASiGdCe coating in vivo.

Results: Through various characterization experiments, we demonstrated that the HASiGdCe coating has suitable microscopic morphology, physical phase characteristics, bonding strength and bioactivity to meet the coating criteria for orthopedic implants. The HASiGdCe coating can release Gd^{3+} and Ce^{4+}, showing strong antibacterial properties against MRSA and PAO-1. The HASiGdCe coating has been shown to have superior osteogenic and angiogenic properties compared to the HA coating in in vitro cellular experiments. Animal implantation experiments have shown that the HASiGdCe coating also has excellent biosafety, antimicrobial and osteogenic properties in vivo.

Conclusion: The HASiGdCe coating confers excellent antibacterial, angiogenic and osteogenic properties on titanium implants, which can effectively enhance implant osseointegration and prevent bacterial infections, and it accordingly has promising applications in the treatment of bone defects related to orthopedic and dental sciences.

Keywords: hydroxyapatite coatings, SiO_2, Gd_2O_3, CeO_2, osseointegration, antibacterial

Introduction

The prevalence of orthopedic diseases, such as tumors, trauma, osteoarthritis and rheumatoid arthritis, has increased yearly over the last few decades. The number of hip replacements rose sharply from 138,700 in 2000 to 310,800 in 2010.[1] The treatment and repair of these orthopedic conditions often places a huge economic burden on society and imposes enormous pressure and difficulty on doctors, which has become a worldwide medical challenge.[2] Titanium (Ti) and its alloys are widely

Received: 20 April 2023
Accepted: 18 August 2023
Published: 6 September 2023

Graphical Abstract

used as artificial implants for hard tissue repair and joint replacement due to their excellent mechanical strength, corrosion resistance, fatigue resistance and biocompatibility.[3,4] However, the biologically inert and stress-shielding effects of titanium implants make them poorly osteoconductive and osteoinductive, which often results in insufficient bonding to bone tissue.[5] In addition, the lack of antibacterial properties of Ti implants makes them susceptible to bacterial infection or biofilm formation, which is another important cause of implant failure.[6,7] It has been reported that approximately 18% of implant failures are can be attributed to aseptic loosening due to inadequate osseointegration, while 20% of failures are attributed to bacterial infection, and some are attributed to both.[8] It is therefore necessary to develop an implant that combines antibacterial properties with osteogenic properties.

An effective method to counter the stress shielding effect and biological inertness of Ti is to apply an osteoconductive coating to its surface, aiming to enhance its ability to bind to bone tissue.[9] Hydroxyapatite (HA) is mainly composed of calcium and phosphate minerals and is widely used as a coating material for metal implants because of its bioactivity and osteoconductivity, which are similar to those of natural human bone.[10] The HA coating inherits the excellent mechanical properties and corrosion resistance of titanium but also promotes the bonding of the implant to the bone tissue and supports uniform inward bone growth.[11] Coating techniques, such as plasma spraying, pulsed laser deposition, laser fusion, bionic solution, electrophoretic deposition, sol-gel and magnetron sputtering deposition, have been reported to be successful in preparing HA coatings on titanium surfaces.[12] Among various coating preparation technologies, atmospheric plasma spraying (APS) technology has the advantages of fast deposition speed, high flame flow temperature, and a wide range of available coating materials. It is the earliest researched and most widely used HA coating preparation process.[13,14] Roy M prepared HA-coated implants that formed significant bone-like surfaces after 2 weeks of implantation, indicating that the HA coating could promote early integration of the implant with the tissue and improve the osteoconductivity and bioactivity of the implant.[15] Nevertheless, HA coatings still lack the osteoinductive ability to enhance bone growth. In addition, HA coatings with good bioactivity inevitably cause problems with bacterial adherence and inflammation, making the anti-microbial properties very limited.[16] As discussed above, the osteoinductivity, proangiogenic capacity, and antibacterial properties of the prepared HA-only coatings are still inadequate, which limits their further application.

An effective solution to address the disadvantages of HA coatings is to add dopants that confer specific functions. The oxides of some functional elements acting as dopants often produce special effects that can greatly improve the performance of HA coatings.[17] Silicon (Si) is considered an essential element for the normal development of bone and connective tissue.[18] It has been shown that silicon induces osteogenic differentiation of MSCs and promotes type I collagen synthesis during the early stages of bone calcification, thereby accelerating osteoid deposition within the osteoid.[19,20]

Many lanthanides have been reported to promote osteogenesis and stimulate bone repair by mimicking the function of calcium in bone minerals.[21,22] For example, it has been shown that gadolinium (Gd), which is mainly deposited in bone tissue, can replace elemental Ca in bone minerals and promote bone deposition.[23] Liao F reported that Gd incorporation could activate the Wnt/β-catenin signaling pathway, promote cell proliferation and upregulate osteogenic genes, such as ALP, Runx2 and Col I, to enhance new bone regeneration.[24] Liu H reported that europium-doped Gd_2O_3 nanotubes can promote osteogenic differentiation and increase bone mineral density by activating the BMP signaling pathway.[25] However, the effect of incorporating Gd_2O_3 into hydroxyapatite coatings on osseointegration and antimicrobial properties is currently unknown. Cerium (Ce), with its powerful antioxidant properties, is another lanthanide element that is highly regarded in bone tissue regeneration engineering.[26] Purohit SD reported that the incorporation of 1000 μg/mL cerium oxide into organic scaffolds enabled efficient free radical scavenging and promoted the proliferation and osteogenic differentiation of MSCs. Cerium oxide has also been shown to have powerful antibacterial effects.[27] Pop OL found that cerium oxide had a significant inhibitory effect on the growth of *Escherichia coli, Salmonella typhimurium, Listeria monocytogenes, Staphylococcus aureus*, and *Bacillus cereus*.[28]

In this study, we designed the first HASiGdCe coating that is effectively osteogenic, antimicrobial and vasculogenic to enhance the osseointegration of titanium implants. First, SiO_2, Gd_2O_3 and CeO_2 nanoparticles were nearly uniformly wrapped around the surface of the HA particle to form a HASiGdCe particle with a micro-nano structure. Then, a composite coating with uniform morphology was prepared on the surface of the titanium substrate using plasma spraying technology. Through various characterization experiments, we demonstrated that the HASiGdCe coating has suitable microscopic morphology, physical phase characteristics, bonding strength and bioactivity to meet the coating criteria for orthopedic implants. We used MC3T3-E1 and HUVECs to investigate the promotion of osteogenic differentiation and angiogenesis by the HASiGdCe coating. In addition, the HASiGdCe coating can continuously release Gd^{3+} and Ce^{4+}, exerting strong antibacterial properties against MRSA and PAO-1. Finally, we used infected animal femur models to investigate the biosafety, antimicrobial and osteointegration properties of the HASiGdCe coating in vivo.

Materials and Methods

The Preparation of Multiple Composite Particles and Their Coatings

In this study, commercial HA particle (Dulai, China), silicon dioxide nanoparticles (SiO_2 NPs) (Macklin, China), gadolinium oxide nanoparticles (Gd_2O_3 NPs) (Desheng, China), and cerium oxide nanoparticles (CeO_2 NPs) (Macklin, China) were used as raw materials. Spherical HA particles were used as the main spraying material, and the nanoparticles were added to the HA particles in different proportions to prepare the three kinds of composite particles, as listed in Table 1.

The pure titanium substrate was roughened in advance by 24 mesh brown corundum blasting under 0.6 MPa pressure. In this work, the APS system (XM-80SK, China) was used to deposit particle formulations to prepare HA, HASi, HASiGd, and HASiGdCe coatings on the titanium surface. The APS process was set up with intermittent cooling, and the temperature of all samples was strictly controlled near 100 °C to reduce the thermal impact on the substrate.[29] All coated samples were prepared with four layers to deposit thick coatings. The APS process parameters are shown in Table 2.

Characterization of Multiple Composite Particles and Their Coatings by Different Techniques

The microstructure and elemental composition of the composite particles and coatings were characterized by field emission scanning electron microscopy (SEM, QUANTA FEG 250, USA) and energy spectrometry (EDS, INCA X-MAX-50, UK).

Table 1 Composition and Size of Particle Formulation (Mass Fraction, Wt%)

Composite Particles	SiO_2 NPs	Gd_2O_3 NPs	CeO_2 NPs	HA	Particle size
HASi	2	0	0	98	15~63μm
HASiGd	2	1	0	97	15~63μm
HASiGdCe	2	1	1	96	15~63μm

Table 2 Processing Parameters of the APS Process

Arc Voltage	Arc Current	Feed Speed	Gun Speed	Spray Distance	Spray Offset
65V	550A	13g/min	100mm/s	120mm	3mm

The roughness values of different coatings were measured by a surface roughness meter (TR200, China). The final results are expressed as the average of the results of five independently repeated experiments. The contact angles of deionized water (DIW) and SBF droplets on the coating surface were measured using a contact angle goniometer (DSA100S, KRUSS, Germany). The final results are expressed as the average of the results of six independently repeated experiments. The phase composition of the coatings was determined using an X-ray diffractometer (XRD, Rigaku DMAX-2500PC, Japan) at 45 kV with a 40 mA current (Cu-Kα radiation source) and diffraction angles from 10° to 80°. Fourier transform infrared spectroscopy (FTIR, Thermo Scientific Nicolet iS20, USA) was used to qualitatively analyze the functional groups of the coatings in the wavenumber range of 400~4000 cm^{-1}.

The Mechanical Properties of Multiple Coatings

The bonding strength between the coating and the substrate was measured according to the standard YY/T 0988.11–2016 for the tensile testing method of calcium phosphate coatings and metal coatings for surgical implant coatings. Four parallel sets of specimens were prepared for each coating. Two specimens were required for each set of tests: a coated specimen for measuring the bonding strength and a paired specimen treated with blasting. The two specimens were then bonded using a high-temperature structural adhesive (Huayi, China). During the bonding process, the axis of the specimen was kept coincident. The bonded samples were placed in a thermostatically heated oven and held at 100 °C for 3 hours for curing. Finally, the bonding strength between the coating and the substrate was measured with a universal tensile tester (INSTRON 8801, USA).

The corrosion behavior of the coated specimens was studied using an electrochemical workstation (Interface 1010E, USA). A 1 cm^2 plasma spray coating was used as the working electrode, a standard calomel electrode (SCE) was used as the reference electrode, and a glassy carbon electrode was used as the counter electrode.[30] SBF solution was used as the electrolyte, and the whole process was carried out at room temperature. The open circuit potential (OCP) was monitored for 3000 s to reach steady state, and then the polarization test was performed from −1 V to 0.5 V (versus OCP) at a scan rate of 1 mV/s.

Bioactivity Analysis and Ion Release of Multiple Coatings in Simulated Body Fluid (SBF)

The coated specimens were immersed in SBF solution (Leagene, China) and incubated in a humidified incubator (37 °C, 5% CO_2), with fresh solution replaced every 24 hours. The surface morphology and chemical composition of the coatings were analyzed at different periods by SEM and EDS, and the bioactivity of the samples was evaluated by studying the formation ability of apatite crystals. The solutions were sampled after 1, 3, 5, 7, 10, 12, and 14 days of incubation. The concentration changes of the ions associated with Gd and Ce released from the composite coating into the SBF were determined by inductively coupled plasma emission spectrometry (ICP–OES/MS, Agilent 7800, USA) to examine the dissolution phenomenon caused by the composite coating.

Antibacterial Tests in vitro

Staphylococcal infections account for nearly 70% of orthopedic implant infections, while *Pseudomonas aeruginosa* infections account for an additional 8%.[31] Gram-positive methicillin-resistant *Staphylococcus aureus* (MRSA, ATCC43300, USA) and the gram-negative opportunistic pathogen *Pseudomonas aeruginosa* (PAO-1, ATCC15442, USA) were used as representative bacteria to verify the antibacterial properties of the different coatings.[32] We evaluated the in vitro antimicrobial properties of different coatings by colony formation assay. Briefly, both types of bacteria were cultured in Luria–Bertani (LB) medium. We inoculated MRSA or PAO-1 suspensions at a density of 10^6 CFU/mL on different coating surfaces. After incubation at 37 °C for 24 h, bacteria attached to the sample surface were eluted using an ultrasonic cleaner (PS-30A, Jiekang, China) at 40,000 Hz. Finally, the eluate was diluted 10,000-fold and spread onto LB agar plates. After incubation at 37 °C for 24 h, the agar plates were imaged, and colonies were counted.

Cell Experiments in vitro

Culture of MC3T3-E1 and HUVECs

MC3T3-E1 (ATCC CRL-2594, USA) cells and HUVECs (ATCC CRL-1730, USA) were cultured in α-MEM/ECM supplemented with 10% fetal bovine serum and 1% penicillin–streptomycin solution.[33] Both types of cells were cultured in a humidified incubator (37 °C, 5% CO_2).

Viability Assessments of MC3T3-E1

A cell counting kit-8 (CCK-8, Biosharp, China) was used to assess the cell proliferation activity of MC3T3-E1 cells on different coating surfaces. Briefly, MC3T3-E1 cells were cultured at a density of 2×10^4 cells/well for 3, 5 and 7 days on different coating surfaces. Afterward, α-MEM and CCK-8 reagents were mixed in a 10:1 ratio and added to each well, and the plates were incubated for 2 hours at 37 °C, protected from light. Then, 100 μL of the suspension was transferred to a 96-well plate. The absorbance was read at 450 nm by an enzyme marker (BMG SPECTROstar Nano2, Germany).[34]

The cytotoxicity of different coatings on MC3T3-E1 cells was assessed by calcein-AM/PI (Solarbio, China). Briefly, MC3T3-E1 cells were inoculated at a density of 2×10^4 cells/well in 24-well plates. The cells were then incubated with different coatings of immersion solution for 3, 5 and 7 days. Thereafter, the cells were incubated with preformulated calcein-AM/PI for 20 min protected from light according to the instructions and observed through an inverted fluorescence microscope (Leica DMI8, Germany).

Alkaline Phosphatase (ALP) Staining and Quantitative Analysis of MC3T3-E1

Alkaline phosphatase (ALP) is an important marker of the early osteogenic differentiation of cells. Therefore, to evaluate the effects of different coatings on the early osteogenic properties of MC3T3-E1 cells, we conducted ALP staining and quantitative analysis of ALP activity.[35] MC3T3-E1 cells were inoculated at a density of 4×10^4 cells/well on the surface of different coatings and stained with a BCIP/NBT alkaline phosphatase staining kit (Beyotime, China) after 7 or 14 days of culture in osteogenic induction medium. Images were captured using a stereomicroscope (Nikon SMZ 745T, Japan). The ALP activity of the cells was measured using an ALP assay kit (Beyotime, China) after 7 or 14 days of culture. Total intracellular protein was also measured using a BCA Protein Assay Kit (Solarbio, China). Finally, the ALP assay results were normalized to the total intracellular protein levels of the samples.

Collagen Secretion Assay of MC3T3-E1

Collagen is one of the most important functional proteins secreted by osteoblasts during bone tissue regeneration, and it is likewise an important marker for assessing the strength of cellular osteogenic properties. Therefore, we evaluated the effect of different coatings on collagen secretion of MC3T3-E1 by Sirius red staining.[36] Briefly, MC3T3-E1 cells were inoculated onto the coated surface at a density of 4×10^4 cells/well and cultured with osteogenic induction medium for 14 days. Next, the samples were rinsed three times with PBS solution, fixed with 4% paraformaldehyde for 30 min and finally stained with Sirius Red stain (Solarbio, China) for 2 h. Images were captured by a stereomicroscope (Nikon SMZ 745T, Japan). For the quantitative analysis of collagen secretion, samples were treated with a decolorization solution (0.1 M NaOH, 200 μL) to dissolve the formed crystals. The OD value of the solution at 540 nm was determined using an enzyme marker (BMG SPECTROstar Nano2, Germany).[37]

Extracellular Matrix Mineralization Assay of MC3T3-E1

The degree of mineralization of the extracellular matrix (ECM) is an important marker of the strength of osteogenic properties of cells at the later stages of osteogenic differentiation. Therefore, we used Alizarin Red S staining to assess the degree of ECM mineralization of MC3T3-E1 cells to observe the late osteoinductivity of different coatings. Briefly, MC3T3-E1 cells were inoculated onto the sample surface at a density of 4×10^4 cells/well. Fourteen days later, the samples were rinsed three times with PBS solution and fixed in 4% paraformaldehyde for 20 min. Subsequently, 500 μL of 2% Alizarin Red solution (Sigma–Aldrich, US) was added to each well, and the plates were incubated for 30 min at room temperature. Images were taken by a stereomicroscope (Nikon SMZ 745T, Japan) after multiple washes of the samples. For quantitative analysis, 10% cetylpyridinium chloride (Sigma–Aldrich, US) was added to each well to

dissolve the calcium deposits on the sample surface. The OD value of the solution was then measured at 562 nm using an enzyme marker (BMG SPECTROstar Nano2, Germany).

Migration Assay of HUVECs

The effect of different samples on the motility and migratory activity of HUVECs was assessed by creating cell scratches. Briefly, HUVECs were inoculated onto 6-well plates at a density of 5×10^5 cells/well. When cell confluence was above 90%, a 200 μL pipette tip was used to scratch a straight line in the middle of each well to create cell scratches. The adherent cells were cultured with different samples of the serum-free soaking solution. Scratches and images were observed and taken after 0, 12 and 24 hours using an inverted microscope (Olympus IX73, Japan).

Tube Formation Assay of HUVECs

Corning Matrigel matrix (BD, USA) was gently added to precooled 48-well plates and solidified at 37 °C for 30 minutes. HUVECs were then inoculated onto the Matrigel matrix at a density of 5×10^4 cells/well and incubated with different samples of the soaking solution. Images were captured at 3 h and 8 h using an inverted light microscope (Olympus IX73, Japan). Finally, the junction and node numbers of vessel rings were quantified by ImageJ software.[38]

Quantitative Real-Time PCR (RT–PCR) Analysis of Osteogenic and Angiogenic Genes

The expression levels of the osteogenic/angiogenic genes ALP, Col I, OCN, Runx2, VEGF, FGFR and eNOS were assessed by RT–PCR. MC3T3-E1 cells or HUVECs were inoculated at a density of 4×10^4 cells/well and cultured on the sample surface for 7 days. Subsequently, total RNA was first extracted using Triquick Reagent (Solarbio, China). The RNA was then reverse transcribed into cDNA using the Evo M-MLV Reverse Transcription Kit (Accurate Biology, China). Finally, we performed RT–PCR on the cDNA using the SYBR Green Pro Taq HS Premix qPCR Kit II (Accurate Biology, China).[39] GAPDH was used to normalize all targeted genes. The primer sequences used are listed in Table 3.

In vivo Animal Experiments

In vivo Implantation Procedures

Thirty male Sprague–Dawley (SD) rats (8 weeks, 250–300 g) were randomly divided into 5 groups (Ti, HA, HASi, HASiGd, and HASiGdCe). The rats were anesthetized using sodium barbiturate prior to implantation. The rat's distal femur was then exposed, and a cylindrical defect (1.2 mm in diameter and 10 mm long) was drilled between the diaphysis and the epiphysis using a surgical drill. A MRSA suspension (10 μL, 10^5 CFU/mL) was then injected into the bone marrow cavity, and groups of implants (1.2 mm in diameter and 10 mm long) were implanted into the defect. Finally, the soft tissue and skin were carefully sutured. The entire implantation procedure was performed under aseptic conditions, and all rats were able to move normally after the operation.

In vivo Antimicrobial Tests

Three days after the implantation procedure, we removed the femur from the rat and gently extracted the implant from the femoral defect. The femoral tissues with defects and implants were immersed in PBS and washed with an ultrasonic cleaner (PS-30A, Jiekang, China) at a frequency of 40,000 Hz for 30 min to completely elute the bacteria attached to the

Table 3 Primers Used in Real-Time PCR

Target Gene	Forward Primer (5′-3′)	Reverse Primer (5′-3′)
ALP	TTGGGCAGGCAAGACACA	GAAGGGAAGGGATGGAGGAG
Col I	GACATGTTCAGCTTTGTGGACCTC	GGGACCCTTAGGCCATTGTGTA
OCN	ACCATCTTTCTGCTCACTCTGCT	CCTTATTGCCCTCCTGCTTG
Runx2	GAACCAAGAAGGCACAGACAGA	GGCGGGACACCTACTCTCATAC
VEGF	GAGGAGCAGTTACGGTCTGTG	TCCTTTCCTTAGCTGACACTTGT
FGFR	AATGAGTACGGCAGCATCAAC	ACCTCGATGTGCTTTAGCCAC
eNOS	GAAGCGAGTGAAGGCGACAA	CCCCATTCCCAAATGTGCT
GAPDH	TGCTGGTGCTGAGTATGTGGT	AGTCTTCTGGGTGGCAGTGAT

surface of the femoral defects and implants. The bacterial eluate obtained in the above steps was diluted 10,000-fold and spread on LB agar plates. The LB agar plates were imaged and counted after incubation at 37 °C for 24 hours. Bacterial infections can induce severe inflammatory reactions in bone tissue and even cause bone loss. To observe the internal organizational structure and inflammatory reaction of the bone tissue around the femoral defect (implant), we performed Giemsa staining on the collected femoral specimens (Solarbio, China).

In vivo Osseointegration Assessment

Four weeks after implantation, the main organs of the rats (heart, liver, spleen, lung and kidneys) were extracted for hematoxylin and eosin (H&E) staining (Solarbio, China) to assess the in vivo biosafety of the different coatings.[40] Four weeks after implantation, the rat femurs were collected and fixed in 4% paraformaldehyde for 2 days and then decalcified in ethylenediaminetetraacetic acid (EDTA, 10 wt%) solution. After gentle removal of the implants, the femurs were dehydrated in ethanol, permeabilized in xylene and embedded in paraffin. Osseointegration around the different coatings was assessed by hematoxylin and eosin (H&E), Masson's trichrome and immunohistochemical (IHC) staining. Finally, images were captured with a microscope (Olympus BX51, Japan).

Statistical Analysis

All data are expressed as the mean ± standard deviation. Statistical analysis was performed by one-way ANOVA and Tukey's multiple comparison test using GraphPad Prism 9.4.1.[41,42] $p<0.05$ was considered statistically significant.

Results and Discussion

The Characterization of Multiple Composite Particles

The microstructure of HA and its composite particle is shown in Figure 1A and 1B). The original morphology of the HA particle is shown in Figure 1A(d), and its slightly rough surface facilitates the adhesion of nanoparticles. Figure 1A(a–c) shows the morphology of the composite particle prepared by mechanical ball milling, and the micron HA particle is not damaged. Figure 1A(a–c) shows that the adhesion of nanoparticles on the surface of HA particles increases with the doping amount, and obvious nanoparticle agglomeration occurs. Combined with the elemental distribution on the surface of the composite particle (Figure 1B), each kind of doped nanoparticle adheres to the HA particle in an approximately uniform manner, forming the HA composite particle with a micro-nano structure.

The Characterization of Multiple Coatings

The morphologies of different coatings on the surface of the titanium matrix are uniformly distributed, showing typical roughening characteristics of plasma spraying (Figure 1C). The coating formed by the melting and accumulation of particles shows mainly aggregated fine particles and smooth and flat coarse particles. The surface of HA coatings is mostly aggregated fine particles, which is attributed to the tendency of droplets to produce spatter and partially melted particles when in contact with the substrate. As a result, the HA coating surface shows the highest roughness (Figure 1E). The HASi coating surface is dominated by flat and coarse particles, which overall are denser and have the lowest surface roughness. This is related to the fact that the added SiO_2 reduces the interlaminar pores and enhances the interlaminar contact. Furthermore, sufficiently large surface tension of nanoparticles can suppress particle splashing to a certain extent. Notably, the nanoparticles possess high-temperature characteristics and fast cooling rates that allow nanostructures to be retained or reformed in the coating by plasma spraying. Thus, the morphology of the nanostructures is dose dependent, and the number of nanoparticles in the coating gradually increases with the addition of other nanodopants, so the surface roughness of the coating also increases.[43] All coatings have micron-level surface roughness, providing a large surface area for new bone formation, which may positively influence cellular behavior and facilitate the enhanced osseointegration of the implants. High-magnification images clearly show the presence of microcracks, holes, and splash droplets in the coating. The surface microcracks are caused by rapid quenching during the plasma spraying process. The holes can provide a highly specific area for subsequent nucleation of calcium phosphate and enhance the bonding strength. During the formation of the composite coating, the doped nanospheres are wrapped on the outside the HA microsphere and flow to the solidified edge of the coarse particles with the spread of the droplets. Thus, nanoparticles

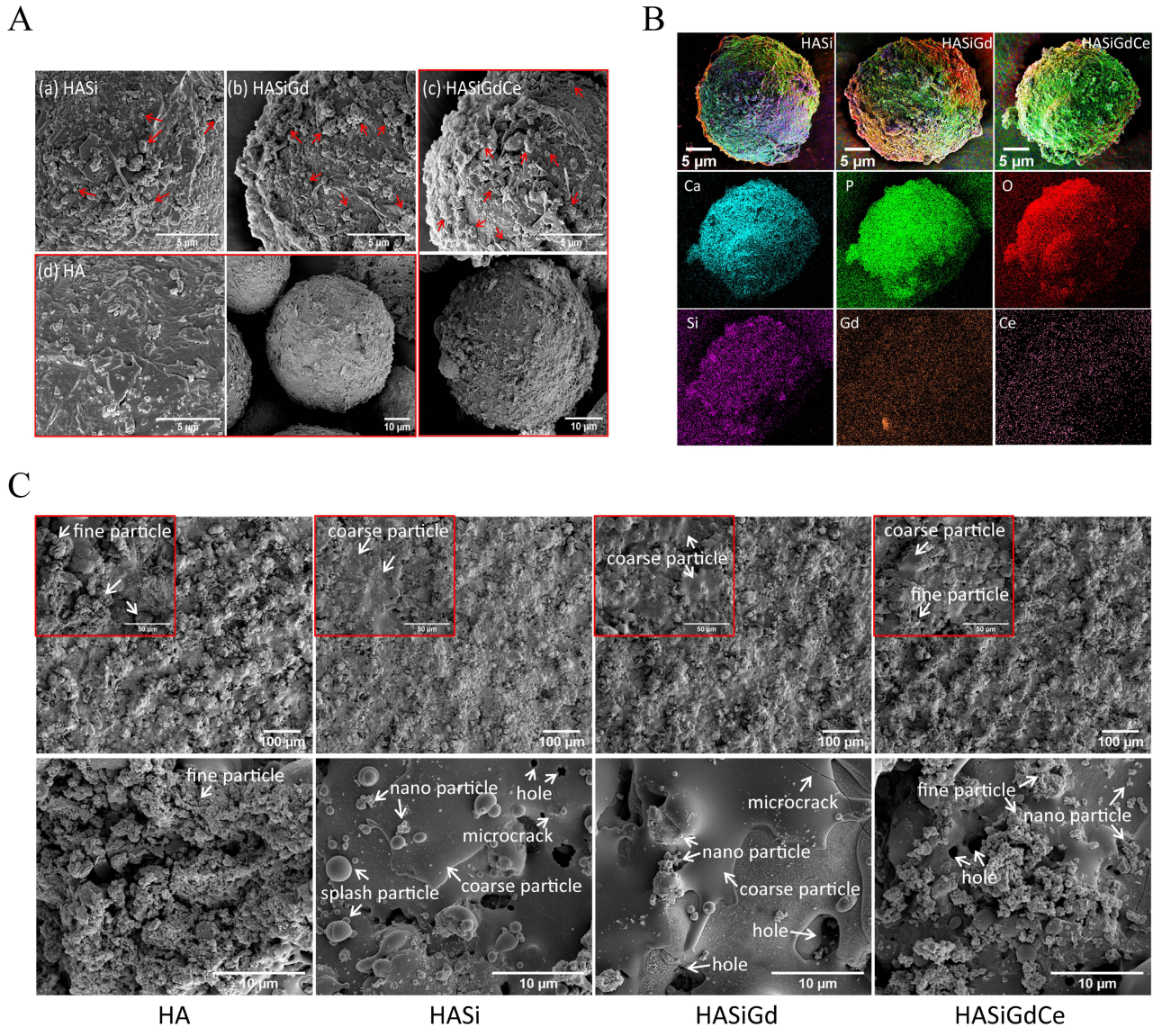

Figure 1 Characteristics of particles and coatings. (**A**) Microscopic morphology of HASi composite particle (a), HASiGd composite particle (b), HASiGdCe composite particle at different magnifications (c), HA particle at different magnifications (d), red arrows indicate nanoparticles on the surface of the composite particles. (**B**) EDS element mapping of composite particles. (**C**) Microstructure of different coatings. (**D**) Cross-sectional morphology of HASiGdCe coating. (**E**) Surface roughness of different coatings, **P < 0.01. (**F**) Contact angles of DIW and SBF droplets on different coating surfaces, **P < 0.01.

distributed at the edges of the flattened coarse particles can be seen in the composite coating. All samples were procedurally sprayed four times to ensure the formation of uniform, flat, and thick coatings. The cross-sectional morphology of the HASiGdCe coating is shown in Figure 1D, and the thickness of the coating is approximately 60 μm.

DIW and SBF droplets exhibited hydrophilic properties on the surface of all specimens (Figure 1F). The contact angles of the coating surfaces are all significantly lower than that of the Ti matrix ($P<0.01$), and the smaller contact angle is an important factor for the implant material to adsorb proteins in vivo, bond with cells, and subsequently promote bone regeneration. The contact angle is mainly influenced by surface morphology, scale, and composition. The contact angle of droplets on the other three coatings is significantly lower than that of the HASiGd coatings ($P<0.01$). The HA coating features a large surface roughness, the lowest contact angle (~12°), and good wettability. This is due to the presence of -OH hydrophilic groups and the large area of micron and submicron structures on the HA surface. Rougher and higher-porosity surfaces have higher surface energy and a greater material contact area.[44] In addition, the microchannel and pore structure can enhance the water absorption effect caused by capillary action and improve the wettability of the coating.

The presence of nanoparticles can significantly affect the morphology of the composite coating. The surface roughness of the HA coating and HASiGdCe coating is significantly higher than that of the HASi coating and HASiGd coating, and the surface roughness of the HASiGd coating is also significantly higher than that of the HASi coating ($P<0.01$). The above results show that the addition of SiO_2 nanoparticles can reduce the surface roughness of the coating, and the doping of Gd_2O_3 and CeO_2 nanoparticles can enhance the surface roughness of the coating. The surface roughness of the composite coating is lower than that of the HA coating, and thus, the surface contact angle is increased. Among the coating surfaces, the roughness of HASiGd is higher, while the contact angle is larger, which may be related to the introduction of Gd ions on the coating surface and the content of nanoparticles.[45] It has also been reported that a contact angle of 40° to 60° is most favorable for cell adhesion.[46] In particular, cell–biomaterial interactions depend mainly on surface composition and morphological features, with rough, hydrophilic and porous surfaces stimulating cell adhesion, proliferation and differentiation as well as extracellular matrix formation.[47] Overall, the HASiGdCe coating has high surface roughness, excellent hydrophilicity, and high surface energy because of the adhesion of nanoparticles on its surface, which can provide favorable conditions for the early adhesion of cells and the growth of cell tissues.

To examine the distribution and content of the coating elements, different areas in the coating were randomly selected for EDS surface scan analysis (Figure 2A). The elements represented by each color are aligned with Figure 1B. The relevant elements of the accessions were detected in each region, and the location distribution of each element was relatively uniform. The mean values of the doped element content in each coating were statistically calculated and compared with the theoretically calculated results, as shown in Figure 2B. The percentage of Si and Gd elements measured in each coating was similar to that of the original doping elements, indicating that the sprayed coating retains the composition of the original particle well. Compared to the original doping content, the measured Ce element content was lower, which may be related to the high density of CeO_2 particles embedded in the interior of the coating or to the low doping volume ratio resulting in poor uniformity of its distribution in the coating.

Phase Composition of Multiple Coatings

To further verify the phase distribution in the coatings, XRD and FTIR spectra of the different coatings were analyzed (Figure 2C and D). The relevant phases of the HA component in the coating are the HA and TCP phases, indicating that the HA particles were overheated and partially decomposed during the APS spraying process. The main components in the HASi coating are HA, TCP, SiO_2, and a small amount of Ti phase. In particular, the only relevant phases of HA and SiO_2 were observed in the X-ray diffractograms of the HASiGd and HASiGdCe coatings, but the elements Gd and Ce could be detected by EDS (Figure 2A and 2B). The content of Gd_2O_3 and CeO_2 in the coating may be excessively low, resulting in the relative diffraction peak intensity being too weak to be detected. Comparing the phase composition and peak intensity of different coatings, especially in the selected region in the figure, indicates that the addition of Gd_2O_3 NPs and CeO_2 NPs causes broadening of the spectral band and enhancement of the spectral peak of the HA-related phase, showing that the crystal content increases and the size decreases during the formation of the coating.[48] The above results show that the sprayed coating retains the characteristics of the original powder well.

The wavelengths of 960~1100 cm^{-1} in the FTIR spectra correspond to the symmetric stretching of the P-O bond (v_1) and the antisymmetric stretching vibrational band (v_3) of the PO_4^{3-} structure. The peaks near wavelengths of 434 cm^{-1} and 470 cm^{-1} correspond to the symmetric bending mode of the P-O bond (v_2). The antisymmetric bending mode (v_4) of the P-O bond was observed at 600 cm^{-1} and 560 cm^{-1}. The above results indicate the presence of the PO_4^{3-} group.[49,50]

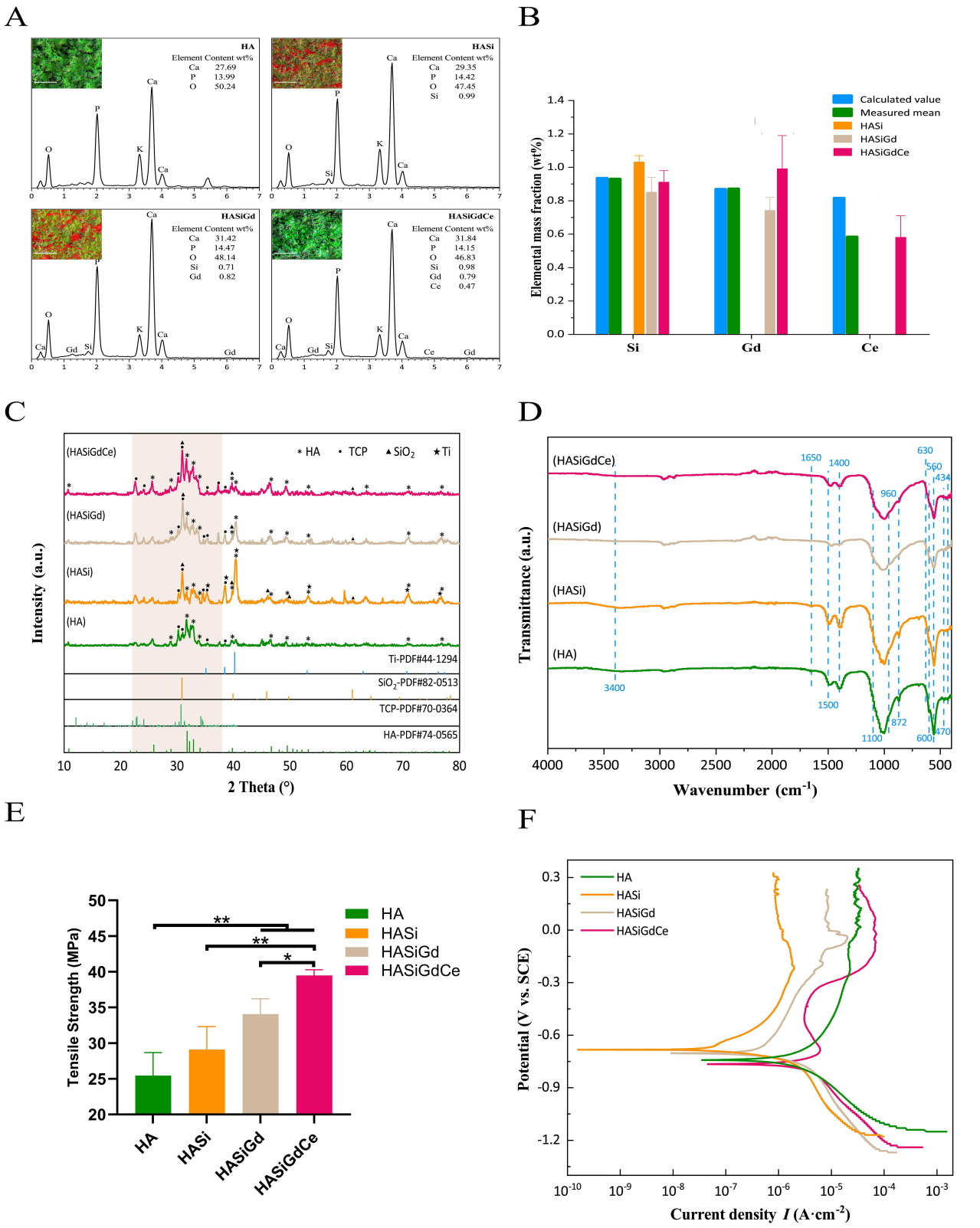

Figure 2 (**A**) EDS mapping of different coating selection areas, scale bar: 200 μm. (**B**) Comparison of calculated and actual measurement results of doped element content in composite coatings. (**C**) XRD patterns of different coatings. (**D**) FTIR spectra of different coatings. (**E**) Bonding strength of different coatings, *P < 0.05, **P < 0.01. (**F**) Tafel curves of different samples in SBF solution.

The weak peak near 1650 cm^{-1} is the characteristic HPO_4^{2-} peak.[51] In addition, the broad band near 3400 cm^{-1} is caused by O-H stretching (v_s), which is characteristic of HA. The weak hydroxyl functional group peak near 630 cm^{-1} indicates the transformation of HA to calcium phosphate and the presence of an amorphous phase, which is consistent with the XRD results. The 1400~1500 cm^{-1} position is a characteristic peak for carbonate ions, as evidenced by an 872 cm^{-1} nearby shoulder strap.[52] CO_3^{2-} can effectively enhance the bonding of the spray coating to the bones and tissues in the simulated body fluids.[53] In addition, with increasing dopant content, the interatomic interactions broadened the characteristic spectra of HA and weakened the peak intensity.

Mechanical Properties of Multiple Coatings

Figure 2E and F shows the results of mechanical property tests for different coatings. The bonding strength of all coatings was above 15 MPa, which is the minimum requirement for HA-coated implants in ISO-13779.[54] The tensile strength of the HASiGdCe coating and HASiGd coating was significantly higher than that of the HA coating ($P<0.01$). The tensile strength of the HASiGdCe coating was significantly higher than that of the HASi coating ($P<0.01$) and the HASiGd coating ($P<0.05$). This indicates that the HASiGdCe coating bonded strongly to the surface of the Ti matrix. Specifically, the average bonding strength of the coating was improved by the addition of nanoparticles. As the nanoparticle content increased, the bonding properties of the coating improved, and the bonding stability increased. This indicates that the addition of nanoparticles enhanced the bonding of the coating. This might be related to the mismatch of thermal expansion coefficients between the doped phase moderated HA coating and the substrate. Moreover, the addition of nanoparticles improved the microstructure of the coating and enhanced the bonding between the coating sheets. The bond strength of the ternary-doped HASiGdCe coating was increased by 55.16% compared to that of the HA coating alone. Further observation of the failure surface, with typical tensile pull-out characteristics, all showed cohesive damage failure, which indicates strong bonding between the coating and the substrate.

According to the polarization curves of different coated samples, the corrosion potential (E_{corr}) and corrosion current density (I_{corr}) were obtained, which can be used to evaluate the corrosion behavior of the samples (Table 4). The corrosion potential of the specimen was ranked HASi > HASiGd > HA > HASiGdCe, and the corrosion current density was ranked HASi < HASiGd < HA < HASiGdCe. In general, samples with better corrosion resistance usually have a lower I_{corr} and higher E_{corr}. The addition of SiO_2 NPs enhanced the corrosion resistance of the coating. Specifically, the SiO_2 NPs reduced the I_{corr} of the coating, implying that the HASi coating had a lower corrosion rate in the corrosive fluid (SBF). Moreover, the high corrosion potential of the HASi coating indicated that it was more difficult for the corrosion reaction to occur, and the degree and likelihood of corrosion were therefore smaller. Notably, the corrosion performance of the coating exhibited a similar trend to the surface roughness (Figure 1D). It is assumed that the denser microstructure of the HASi coating reduces the contact area with the corrosive solution and enhances the shielding effect, thus effectively protecting the substrate from corrosion. In addition, the corrosion current density of the composite coating gradually increased with the addition of other nanoparticles. The surface characteristics of the rough coating with pores, microcracks and fine particles increased the immersion area and dissolution rate of the coating in solution, which may be the reason for the increased corrosion rate. In particular, the HASiGdCe coating was also prone to corrosion due to its abundant particle content and greater particle exchange with the SBF solution.

Table 4 Corrosion Parameters of Different Samples

Sample	Corrosion Potential E_{corr} (mV))	Corrosion Current Density I_{corr} ($\mu A\ cm^{-2}$)
HA	−741.6	2.944
HASi	−682.6	1.644
HASiGd	−702.5	2.713
HASiGdCe	−765.2	3.091

The Bioactivity and Ion Release of Multiple Coatings

Considering that the formation process of the apatite layer on the coating surface is similar, HA material is recognized as a bioactive coating material. In this paper, HASiGdCe, which has the highest content of additional components, is used as an example to characterize the bioactivity of the coating. Figure 3A shows the microscopic morphological changes of the HASiGdCe coating after SBF immersion. The morphology of the apatite layer generated on the coating surface was closely related to the immersion time.[55] The formation of apatite layers began with the nucleation of small particles, and rough locations, such as melt-drop edges, pores, and microcracks, were the preferred nucleation sites. As the incubation time increased, the rough surface of the coating was continuously dissolved, while the locations of pores and microcracks were filled with newly formed apatite layers, showing a dune morphology consisting of spherical grains. The surface of the coating immersed for 5 days was mostly covered by the growing apatite layer, indicating that the coating had high biological activity. The dune apatite showed a multilayered accumulation morphology, which was caused by its crystallization and continuous growth starting from small areas at different heights on the rough HA coating surface. With increasing incubation time in SBF, the size of the spherical dune morphology and the accumulation density gradually increased, and the surface also contained some micropores and microcracks generated by the coating reaction and diffusion of some ions with the simulated fluid. Given enough time, the entire surface was covered by this new structure made up of small particles.

Different areas of the coating surface were selected to test the element distribution and calculate the average content variation, as shown in Figure 3B and C). The elements Ca, P, and O, which are essential basic elements necessary for the formation of apatite layers by precipitation, were detected on each surface after immersion in SBF. The elemental contents of Si, Gd, and Ce on the coating surface gradually decreased with increasing incubation time. On the one hand, these elements were consumed by ion release and auxiliary reactions; on the other hand, the newly formed apatite layer had an encapsulation effect on the nanoparticles on the coating surface.

As shown in Figure 3D, the release of both Gd and Ce ions from the HASiGdCe coating into SBF showed similar decreasing trends overall, except for a slight increase in the fluctuation of Gd ion release on day 12. With increasing immersion time, the ion release showed a significant decrease at first, and then the rate of release gradually slowed. This

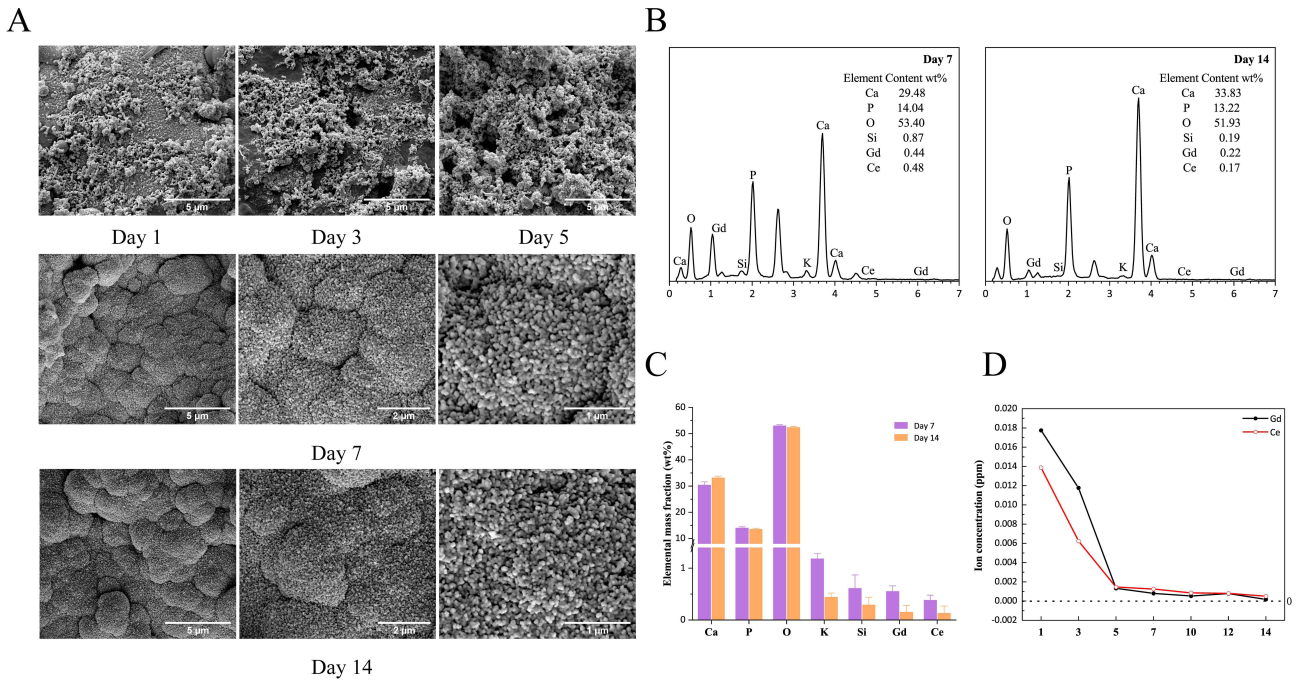

Figure 3 HASiGdCe coating immersed in SBF for different durations. (**A**) Coatings morphology at the different duration of immersion. (**B**) EDS of coatings at the different duration of immersion. (**C**) Elemental content and the statistical average of HASiGdCe coating surface after SBF immersion. (**D**) The release of Gd and Ce ions in SBF at different periods.

was related to the content of particles on the coating surface, the reaction with the solution, and the formation of the apatite layer. Day 5 was the inflection point for the change in the rate of release of both ions. Based on the above observations of the surface morphology of the coating, it can be confirmed that the integrity of the newly formed apatite layer has an inhibitory effect on ion release. The above results indicate that the ternary-doped HASiGdCe composite coating shows good bioactivity.

In vitro Antibacterial Properties of Multiple Coatings

Bacterial infection-induced peri-implantitis leads to rapid bone loss around the implant and is one of the main causes of implant failure. Thus, the antimicrobial properties of implants are crucial for their repair of bone defects and prevention of postoperative infections.[56] We used MRSA and PAO-1 as representative bacteria and counted their CFUs using the spread plate method to evaluate the in vitro antimicrobial properties of the HASiGdCe coating. The LB agar plate images are shown in Figure 4A. For both MRSA and PAO-1, the number of colonies in the HASiGd and HASiGdCe groups was significantly less than that in the HA and HASi groups. However, the number of colonies in the HASiGdCe group was the lowest. The results of their further quantitative analysis are shown in Figure 4B. The colony counts of MRSA/PAO-1 for HASiGd and HASiGdCe were 144±12/345±30 and 82±9/186±21, respectively, which were significantly lower than those for HA (248±17/623±9) and HASi (222±8/550±14) ($P<0.01$). Moreover, the antimicrobial activity of HASiGdCe was significantly higher than that of HASiGd ($P<0.01$). However, the antimicrobial activity of HA was similar to that of HASi. Therefore, we can conclude that the HASiGdCe coating may have very strong antimicrobial properties against both gram-positive and gram-negative bacteria. The reason for its strong antimicrobial properties is that the introduction of Gd_2O_3NPs and CeO_2NPs enables it to release Gd^{3+} and Ce^{4+} into the

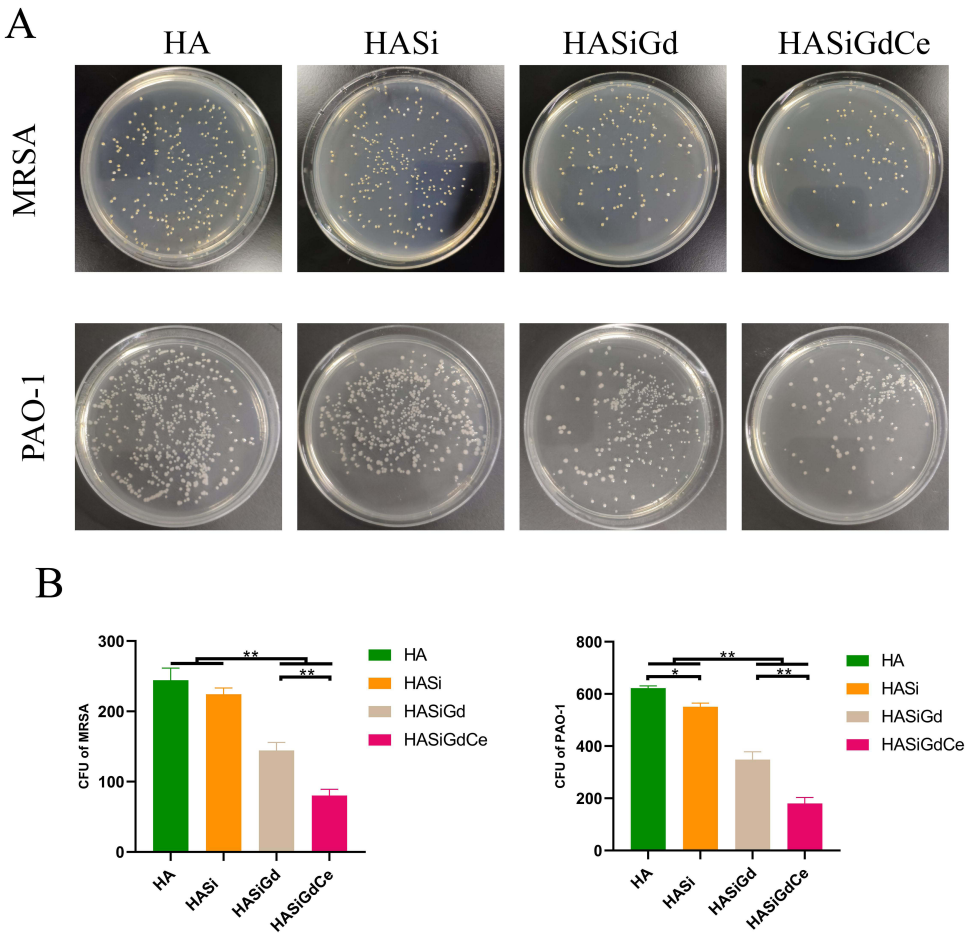

Figure 4 Results of antibacterial testing. (**A**) Images of cultivated MRSA and PAO-1 colonies on LB agar plate. (**B**) statistics of MRSA and PAO-1 colony-counting on different samples at 24 h. *P < 0.05, **P < 0.01.

environment. Combined with previous studies, the mechanism of bacterial killing by Gd^{3+} and Ce^{4+} may be by inducing abnormal responses such as oxidative stress, altered heterogeneity, changes in cell membrane permeability, disturbances in electrolyte homeostasis, enzyme inhibition, protein inactivation, and altered gene expression, which ultimately leads to bacterial death.[22,28] However, this mechanism still needs to be confirmed by further experiments, which is the direction of our future research.

Cytocompatibility of Multiple Coatings

Excellent biocompatibility is a prerequisite for the future clinical application of implantable biomaterials. At the same time, good cytocompatibility is the basis for the excellent osteogenic and angiogenic activity of implantable materials.[57] We used CCK-8 assays and live/dead cell staining to assess the cell proliferative activity and cytotoxicity of different coatings, including HA, HASi, HASiGd, and HASiGdCe. The results of the CCK-8 assays are shown in Figure 5A. The proliferative activity of MC3T3-E1 cells on the surface of different samples did not differ significantly on Days 3 or 5 ($P>0.05$). This suggests that HASiGdCe shows excellent cytocompatibility at an early stage. Until Day 7, the cell proliferation activities of HASi, HASiGd and HASiGdCe were increased compared to those of the HA and Ti groups. In contrast, there were no significant differences between HASi, HASiGd, and HASiGdCe ($P>0.05$). This indicates that the HASiGdCe coating may promote the proliferation of MC3T3-E1 cells over time, which is mainly due to the introduction of SiO_2NPs. However, the presence of Gd_2O_3NPs and CeO_2NPs did not make it toxic to the cells.

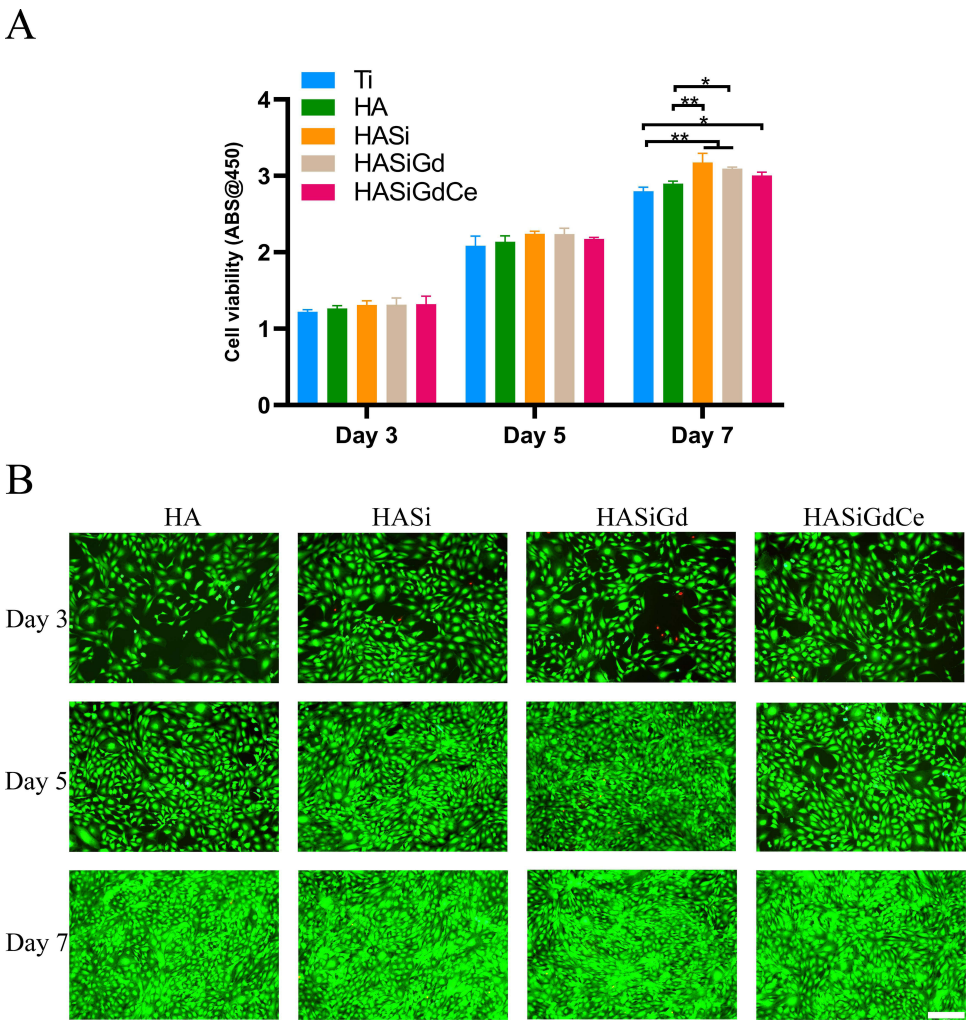

Figure 5 (**A**) Cell viability of MC3T3-E1 evaluated by CCK-8 assay. (**B**) Fluorescence images of calcein-AM/PI staining of MC3T3-E1, scale bar: 200 μm. *P < 0.05, **P < 0.01.

After calcein-AM/PI staining, live cells emit green fluorescence, and dead cells emit red fluorescence, so we used live/dead cell fluorescence staining to determine the cytotoxicity of HASiGdCe. The results of live/dead cell staining are shown in Figure 5B. Under fluorescence microscopy, all groups of MC3T3-E1 cells largely fluoresced green and rarely fluoresced red, showing excellent biocompatibility. This further suggests that the HASiGdCe coating has excellent cytocompatibility and that the introduction of SiO_2NPs, Gd_2O_3NPs and CeO_2NPs does not cause toxicity to cells.

In vitro Osteogenic Properties of Multiple Coatings

The in vitro osteoinductivity of the multiple coatings was assessed by examining ALP activity, collagen secretion levels, ECM mineralization and expression levels of osteogenesis-related genes (ALP, Col I, OCN and Runx2) in MC3T3-E1 cells. ALP activity is an important indicator of early osteogenic differentiation and bone metabolism in preosteoblasts.[58] Therefore, we analyzed the early osteoinductivity of multiple coatings using ALP staining and quantitative ALP activity assays. The results of ALP staining are shown in Figure 6A, in which the positive staining area of the same group of coatings increased in a time-dependent manner from 7 to 14 days. More significantly, the positively stained areas of HA, HASi, HASiGd, and HASiGdCe appeared to be sequentially higher at the same time points. The results of the quantitative ALP activity assay are shown in Figure 6B and are fully consistent with the ALP staining results. The above results indicate that the HASiGdCe coating has

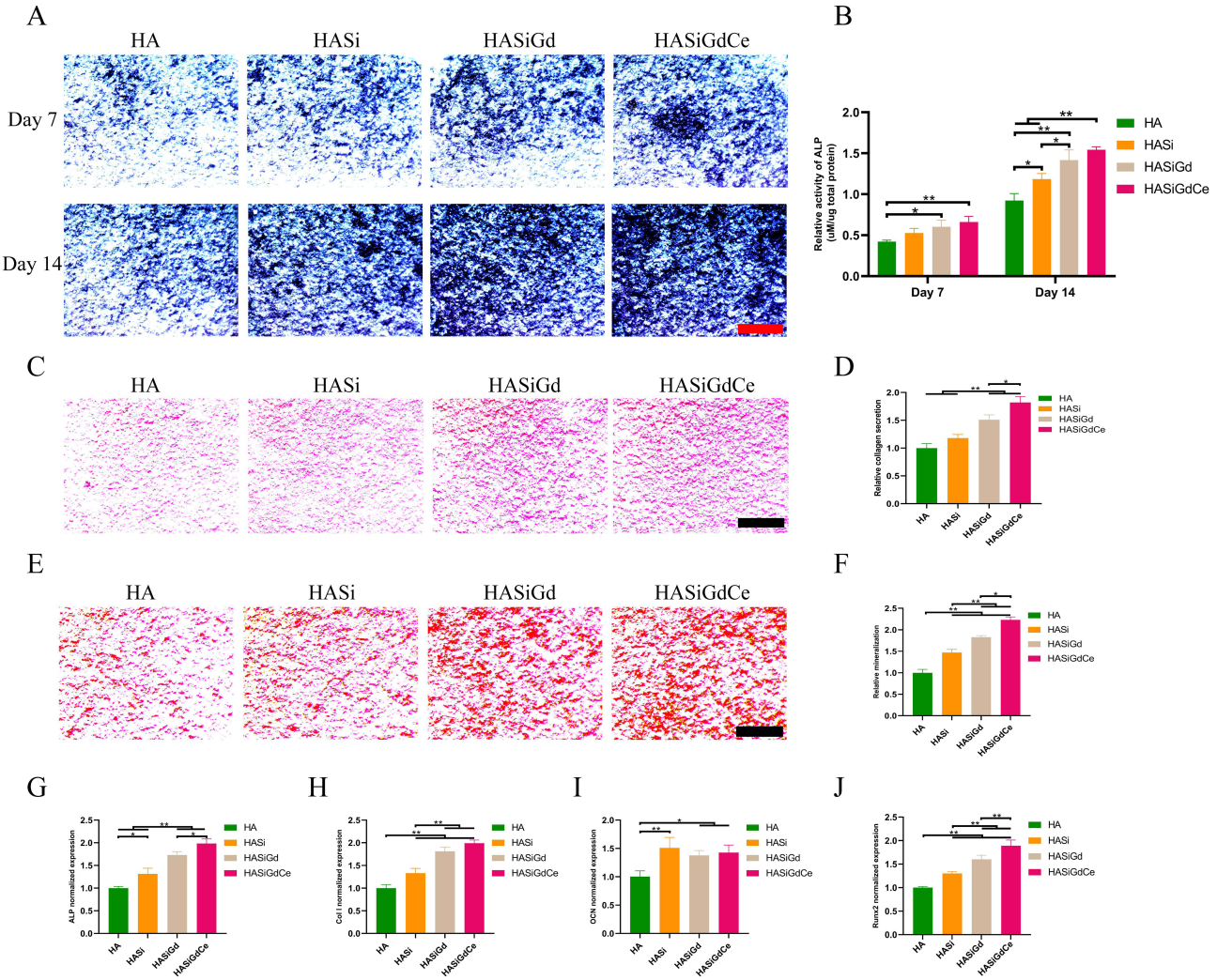

Figure 6 Results of osteogenic properties studies. (**A**) ALP staining images of different coatings. (**B**) Quantitative analysis of ALP activity. (**C**) Sirius red staining images of different coatings. (**D**) Quantitative analysis of collagen secretion. (**E**) Alizarin red S staining images of different coatings. (**F**) Quantitative analysis of ECM mineralization. The relative expression levels of ALP (**G**), Col I (**H**), OCN (**I**) and Runx2 (**J**) in MC3T3-E1 assessed by RT-PCR, GAPDH was used as control. Scale bar: 500 μm. *P < 0.05, **P < 0.01.

optimal osteogenic activity at the early stage of osteogenesis. The introduction of SiO_2NPs, Gd_2O_3NPs and CeO_2NPs enhances the osteoinductive properties of hydroxyapatite coatings at an early stage.

Collagen is one of the most important functional proteins secreted by osteoblasts during bone tissue regeneration and can accelerate bone deposition within osteoids. Therefore, its secretion level is an important indicator for assessing the strength of the osteogenic properties of the cells. We assessed the effect of multiple coatings on collagen secretion from MC3T3-E1 cells by Sirius red staining. The results of Sirius red staining are shown in Figure 6C, and the positive staining areas of HA, HASi, HASiGd, and HASiGdCe likewise appeared to be sequentially elevated. Related quantitative analysis is shown in Figure 6D. The collagen secretion in the HASi, HASiGd and HASiGdCe groups was 1.18, 1.51 and 1.82 times higher than that in the HA group. The above results indicated that the introduction of SiO_2NPs, Gd_2O_3NPs and CeO_2NPs could elevate the collagen secretion level of MC3T3-E1 cells, which in turn promoted their osteogenic differentiation.

The degree of ECM mineralization can reflect the level of late osteogenic differentiation of preosteoblasts.[59] We assessed the degree of ECM mineralization in MC3T3-E1 cells by Alizarin Red S staining to observe the late osteoinductivity of multiple coatings. The results of Alizarin Red S staining are shown in Figure 6E, and the largest number of mineralized nodules (red areas) were found on the surface of the HASiGdCe coating. The quantitative analysis of ECM mineralization is shown in Figure 6F, and the levels of ECM mineralization in the MC3T3-E1 of the HASi, HASiGd, and HASiGdCe groups were 1.47-fold, 1.83-fold, and 2.23-fold of those of the HA group. The above results indicate that the HASiGdCe coating also has optimal osteoinductivity at the late stage of osteogenic differentiation. The addition of SiO_2NPs, Gd_2O_3NPs and CeO_2NPs can promote the late osteoinductivity of hydroxyapatite.

ALP, Col I, OCN and Runx2 are recognized osteogenesis-related genes that play key roles in cellular osteogenic differentiation as well as bone formation and reconstruction. Therefore, we quantified the expression levels of ALP, Col I, OCN and Runx2 in MC3T3-E1 cells by RT–PCR to further evaluate the osteoinductive properties of the HASiGdCe coating. The results of RT–PCR are shown in Figure 6G–J). For ALP, Col I and Runx2, the gene expression levels of HA, HASi, HASiGd and HASiGdCe showed a sequential increase. For OCN, the gene expression levels of HASi, HASiGd and HASiGdCe were similar ($P>0.05$), but all of them were higher than those of the HA group ($P<0.05$). Compared with HA, HASiGdCe increased the expression levels of ALP, Col I, OCN and Runx2 by 1.98-fold, 1.99-fold, 1.43-fold and 1.89-fold, respectively. In conclusion, the RT–PCR results further demonstrated that the HASiGdCe coating has excellent in vitro osteoinductive properties.

After analyzing the above experimental results, we concluded that the excellent osteogenic activity of the HASiGdCe coating can be attributed to the ingenious introduction of SiO_2NPs, Gd_2O_3NPs and CeO_2NPs. The introduction of SiO_2NPs provided bone tissue regeneration with an appropriate amount of silicon. As an important trace element in bone tissue formation, silicon can induce osteoblasts to undergo proliferation and differentiation, promote the production and secretion of type I collagen, and accelerate bone deposition within osteoids.[19,20] The introduction of Gd_2O_3NPs and CeO_2NPs allows the coatings to release moderate amounts of Gd^{3+} and Ce^{4+}. Elemental Gd and Ce, as lanthanides, have been reported to stimulate the regeneration and repair of skeletal tissues by mimicking the function of elemental calcium in bone minerals.[21,23] In addition, elemental Ce has a powerful antioxidant function: it can efficiently scavenge free radicals in bone defects and promote cell proliferation and osteogenic differentiation.[26,27] However, there are still limitations in our current exploration of the osteogenic mechanism of the HASiGdCe coating. Considering that the HASiGdCe coating can promote the elevated expression levels of the ALP, Col I, OCN, and Runx2 genes, we speculate that it may promote bone tissue regeneration by activating the Wnt/β-catenin signaling pathway. However, this still needs to be further explored and will be the direction of our future research.

In vitro Angiogenic Properties of Multiple Coatings

Angiogenesis is considered a prerequisite for implantable biomaterials to achieve osseointegration. The angiogenic activity of the implant coating is essential for it to achieve osseointegration.[60] Therefore, we assessed the in vitro angiogenic activity of multiple coatings by migration assay, tube formation assay, and RT–PCR analysis of angiogenic genes of HUVECs. The motility and migration of HUVECs is an important indicator of their angiogenic ability. We evaluated the effect of the HASiGdCe coating on the migratory activity of HUVECs by creating cell scratches. The results of the HUVEC migration assay are shown in Figure 7A and B). At both 12 h and 24 h, the most obvious cell

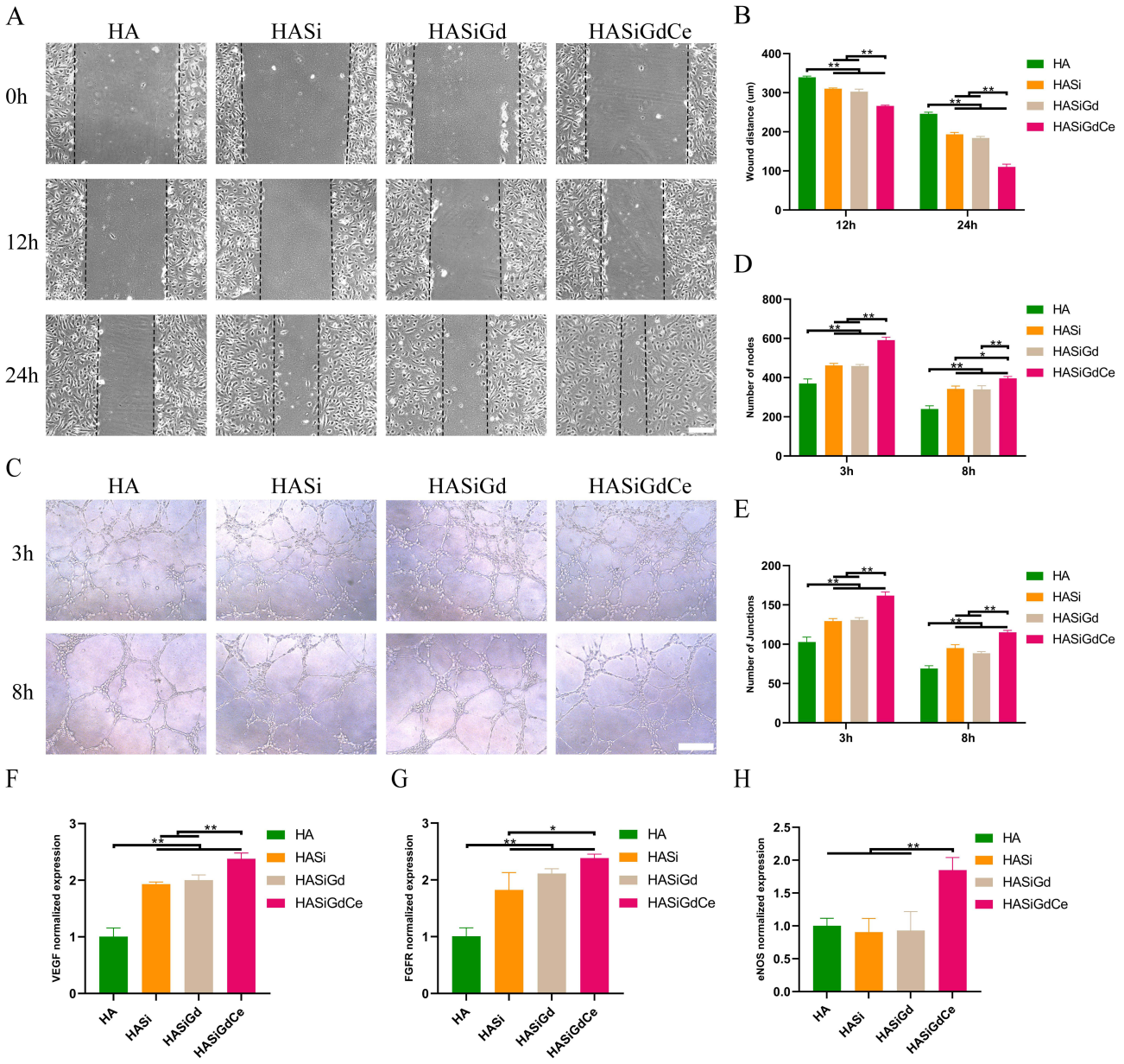

Figure 7 Results of angiogenic Properties studies. (**A**) Images of migration of HUVECs at 0h, 12 h and 24 h, scale bar: 100 μm. (**B**) Quantitative analysis of HUVECs migration at 12h and 24h. (**C**) Images of HUVECs tube formation after incubation for 3 and 8 h, scale bar: 200 μm. (**D**) Quantitative analysis of tube formation by means of node numbers. (**E**) Quantitative analysis of tube formation by means of junction numbers. The relative expression levels of VEGF (**F**), FGFR (**G**), eNOS (**H**) in HUVECs assessed by RT-PCR, GAPDH was used as control. *P < 0.05, **P < 0.01.

migration phenomenon was observed in the HASiGdCe group (P<0.01). The migration activities of HUVECs in the HASi and HASiGd groups were comparable, but both were greater than that in the HA group. Notably, the cell scratches in the HASiGdCe group were close to completely healed after 24 h. The above results demonstrated that the HASiGdCe coating has strong pro-cell migration activity due to the introduction of SiO_2NPs and CeO_2NPs.

Endothelial cell tube formation is an important step in angiogenesis in bone regeneration, and it is also an important measure of the angiogenic activity of HUVECs. The tube formation images of HUVECs and their associated quantitative analyses are shown in Figure 7C–E). First, at 3 h, we observed a relatively large number of short and simple cellular tubes forming in all groups. By 8 h, the number of endothelial nodes and junctions in each group decreased compared to that at 3 h because the HUVECs formed a complex and tightly connected network of large blood vessels. However, HASiGdCe showed the most significant proangiogenic ability at both 3 h and 8 h (*P<0.01*). The proangiogenic abilities

of HASi and HASiGd were relatively similar overall (*P>0.05*), but both were significantly higher than that of HA (*P<0.01*). Therefore, we suggest that the introduction of SiO_2NPs and CeO_2 NPs may be able to enhance the angiogenic ability of HUVECs.

The expression levels of angiogenesis-related genes (VEGF, FGFR and eNOS) were quantified by RT–PCR (Figure 7F–H)). The expression levels of VEGF and FGFR were highest for HASiGdCe, while those for HASi and HASiGd were similar *(P>0.05)*, and all three groups exhibited higher expression of VEGF and FGFR than the HA group (*P<0.01*). The expression levels of eNOS were similar for HA, HASi and HASiGd (*P>0.05*), and all three groups had lower eNOS expression than the HASiGdCe group (*P<0.01*). In conclusion, the HASiGdCe coating upregulates all our selected target genes and probably shows the best performance in terms of angiogenesis.

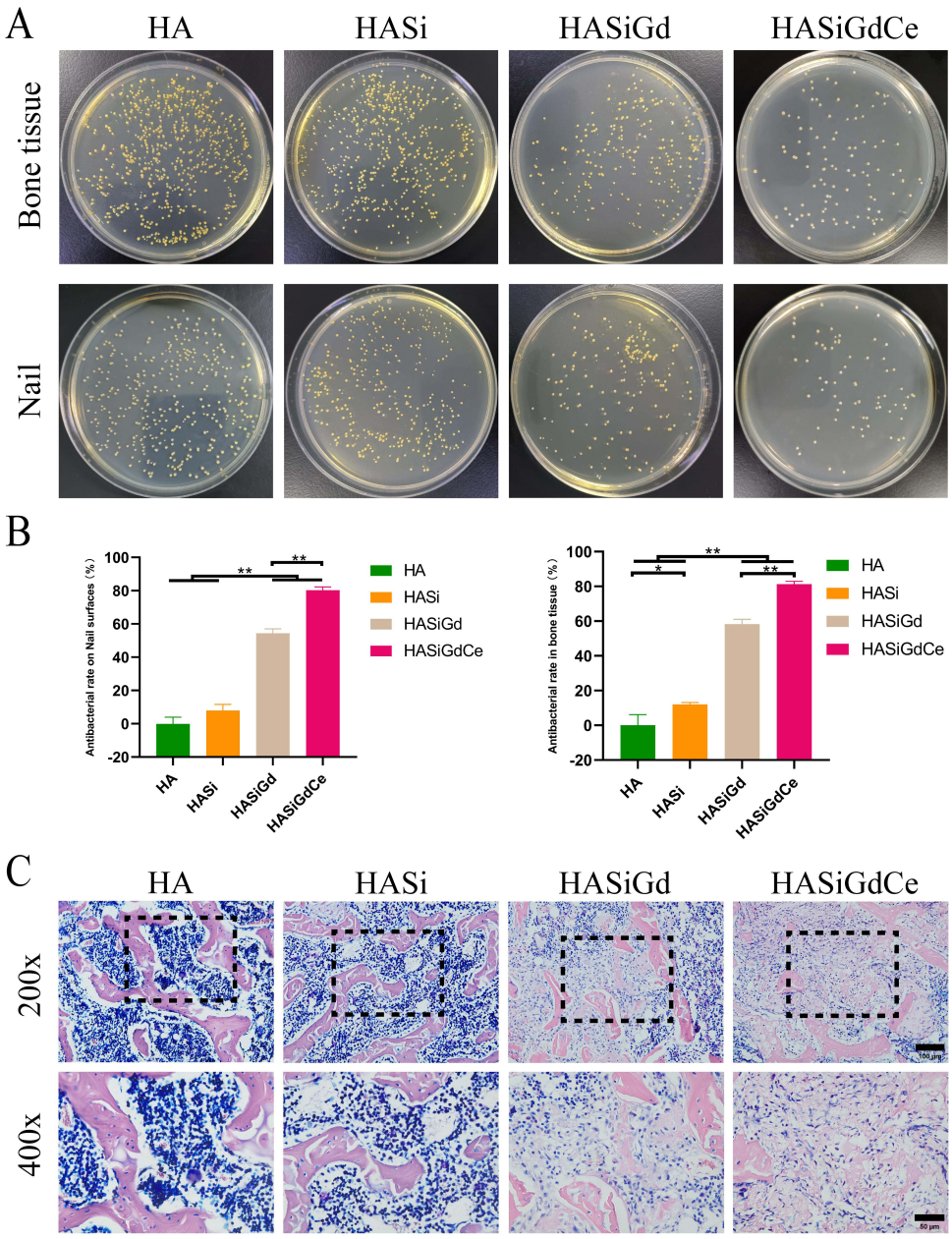

Figure 8 (**A**) The agar plate images of residual MRSA colonies in bone tissue and nail. (**B**) Quantitative analysis of antimicrobial rates of residual MRSA colonies in bone tissue and nail. (**C**) Giemsa staining images of different groups of bone tissue, scale bar: 100 μm / 50 μm.*P < 0.05, **P < 0.01.

After analyzing the above experimental results, we concluded that the excellent angiogenic activity of the HASiGdCe coating can be attributed to the introduction of SiO_2NPs and CeO_2NPs. According to previous reports, SiO_2NPs may promote cell adhesion, proliferation, migration, and angiogenesis by upregulating the expression levels of growth factors such as vascular endothelial growth factor-α, hypoxia inducible factor-1α, angiopoietin-1, and nesprin-2 in vascular endothelial cells.[61] CeO_2NPs possess free radical quenching properties, which can regulate the intracellular oxygen environment to induce angiogenesis while protecting vascular endothelial cells from adverse oxidative stress.[62] However, the specific molecular mechanisms and signaling pathways by which the HASiGdCe coating promotes angiogenesis still need to be further explored and are also the direction of our future research.

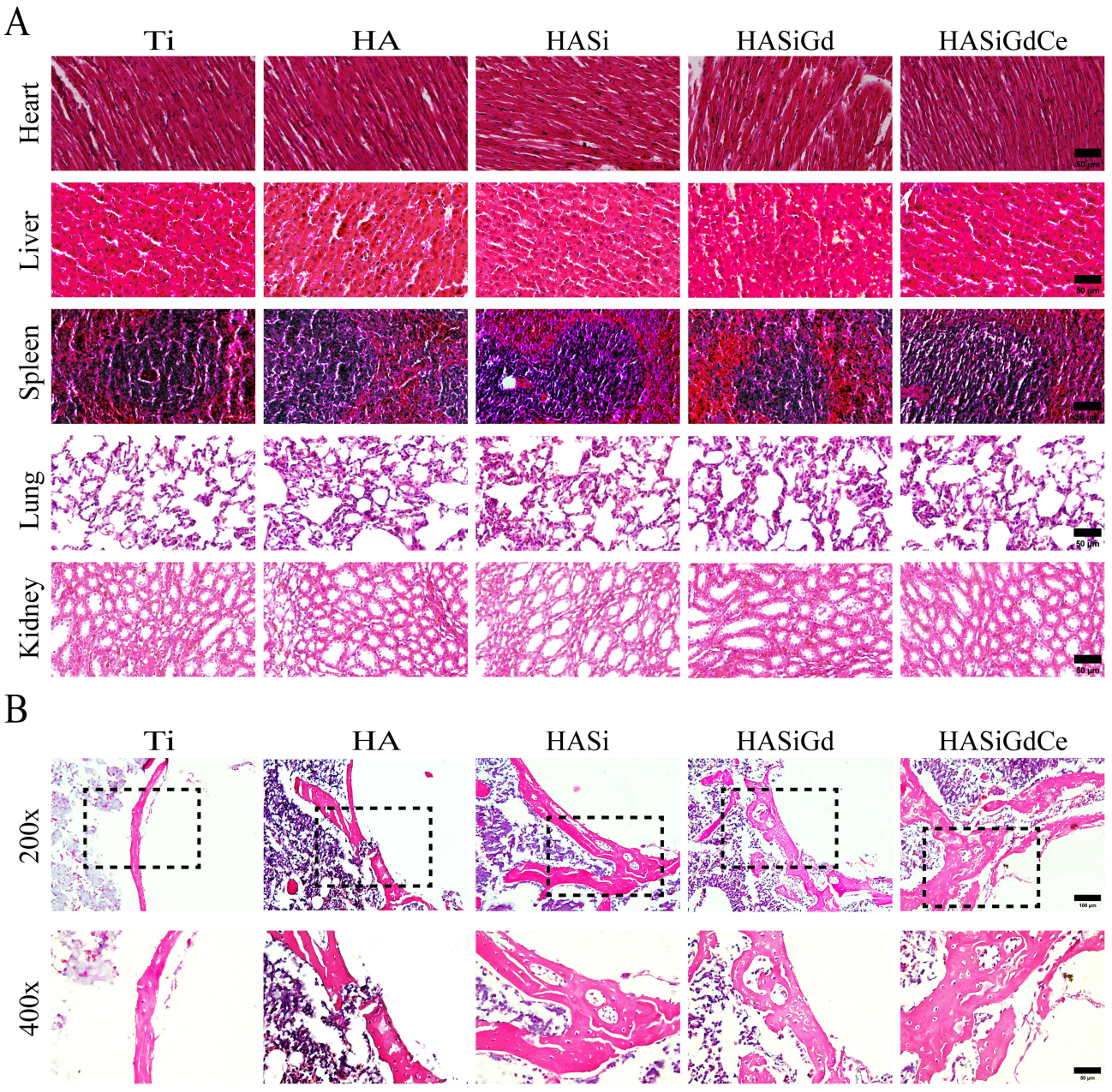

Figure 9 (**A**) H&E staining images of the heart, liver, spleen, lungs and kidneys of rats, scale bar: 50 μm. (**B**) H&E staining images of different groups of bone tissue, scale bar: 100 μm / 50 μm.

In vivo Antibacterial Properties of Multiple Coatings

The antimicrobial properties, biosafety and osseointegration of the coating in vivo were further assessed using a rat model of MRSA infection. Three days after implantation, residual bacteria on the bone tissue and nail were collected and counted for analysis by a standardized plate counting method. LB agar plate images are shown in Figure 8A. For both the bone tissue surface and nail surface, the number of colonies in the HASiGd and HASiGdCe groups was significantly less than that in the HA and HASi groups. The number of colonies in the HASiGdCe group was the lowest. The quantitative analysis of the antimicrobial rate is shown in Figure 8B. On the surface of bone tissue, the antimicrobial rates of the HASiGd and HASiGdCe coatings were as high as 58.30% and 81.26%, while that of the HASi coating was only 12.10%. On the nail surface, the antimicrobial rates of the HASiGd and HASiGdCe coatings were as high as 54.37% and 80.35%,

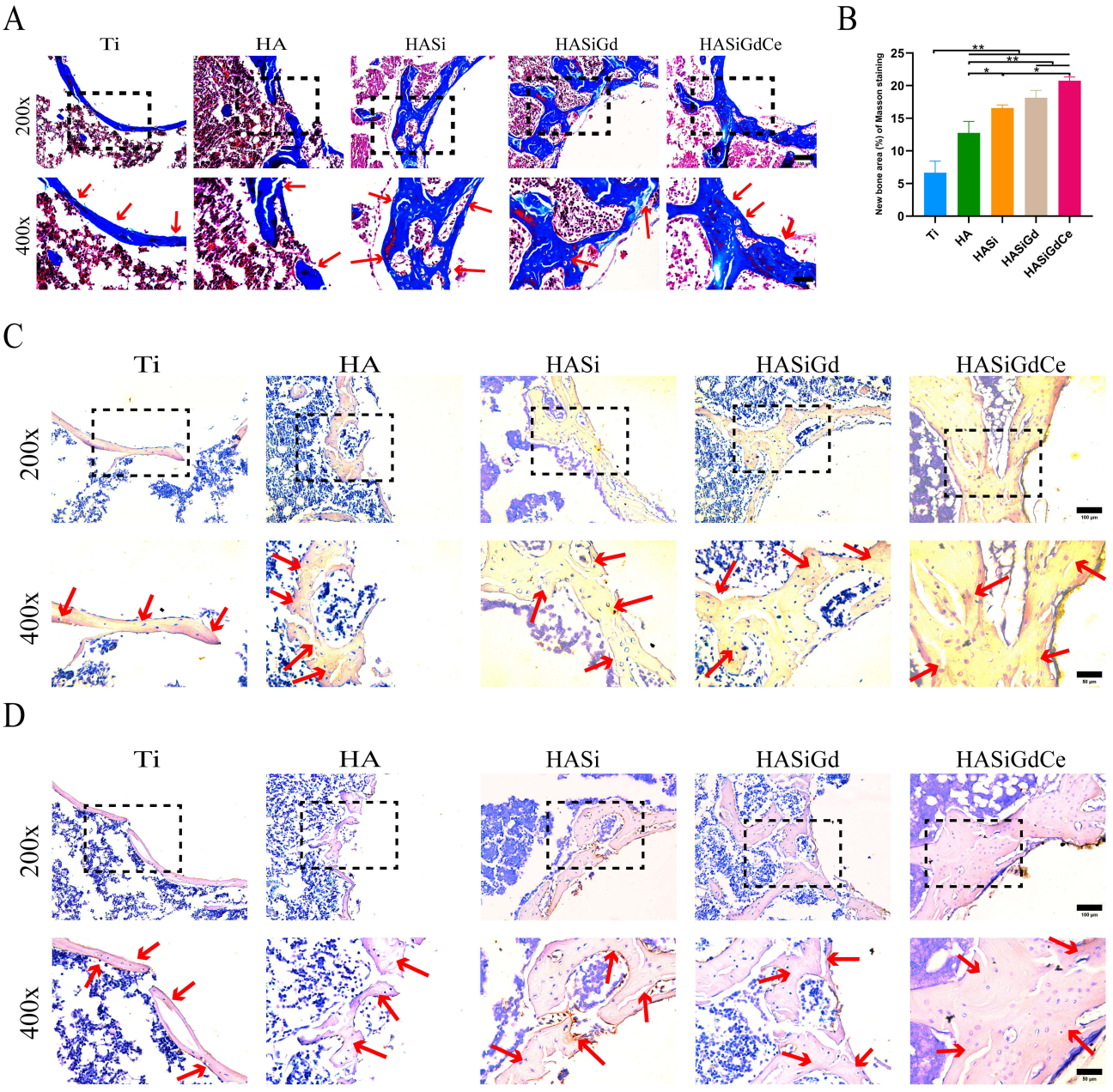

Figure 10 (**A**) Masson's trichrome staining images of different groups of bone tissue, red arrows indicate the important staining areas. (**B**) Quantitative analysis of Masson's trichrome staining, *P < 0.05, **P < 0.01. (**C**) Immunohistochemical staining images of the osteogenesis-related protein OCN, red arrows indicate the important staining areas. (**D**) Immunohistochemical staining images of the osteogenesis-related protein Col I, red arrows indicate the important staining areas. Scale bar: 100 μm / 50 μm.

while that of the HASi coating was only 7.91%. This was consistent with the results of in vitro antimicrobial experiments, further indicating that the excellent antimicrobial properties of the HASiGdCe coating are due to the introduction of Gd_2O_3NPs and CeO_2NPs, which enable the release of Gd^{3+} and Ce^{4+} in the environment. In addition, to assess the residual bacterial and inflammatory status of the bone tissue, we performed Giemsa staining on the collected femoral specimens (Figure 8C). More severe inflammatory cell infiltration and more residual bacteria were observed in specimens from the HA and HASi groups than in specimens from the HASiGd and HASiGdCe groups. Few inflammatory responses to bacterial infection were detected in specimens from the HASiGdCe group, further demonstrating the excellent antimicrobial and anti-inflammatory ability of the HASiGdCe coating.

In vivo Osseointegration Properties of Multiple Coatings

Good biosafety of the implant coating is a prerequisite for excellent osseointegration. Four weeks after implantation, we performed H&E staining analysis of the major rat organs (heart, liver, spleen, lungs and kidneys) to assess the in vivo biosafety of the HASiGdCe coating. The results showed that the HASiGdCe coating has negligible tissue toxicity and does not induce pathological abnormalities or damage in rats, demonstrating good in vivo biosafety (Figure 9A).

We performed H&E, Masson's trichrome and immunohistochemical (IHC) staining on femoral specimens to assess osseointegration around the different coatings. In the results of H&E (Figure 9B) and Masson's trichrome staining (Figure 10A), more mature and thicker new bone matrix was observed around the HASiGdCe coating. Quantitative analysis of Masson's trichrome staining revealed that the HASiGdCe group had the highest percentage of new bone formation area (20.75%), followed by HASiGd (18.15%), HASi (16.56%), HA (12.77%) and Ti (6.65%) (Figure 10B). The expression levels of osteogenic-related proteins (OCN and Col I) were further assessed by immunohistochemical staining (Figure 10C and D)). The largest area of positive staining was observed in the HASiGdCe samples, indicating that the HASiGdCe coating has the best osteogenic properties. In summary, the HASiGdCe coating has the best in vivo antimicrobial properties and osseointegration capabilities and is a highly promising surface coating for titanium implants.

Conclusion

In this study, we doped SiO_2NPs, Gd_2O_3 NPs, and CeO_2 NPs into HA and then successfully prepared a multifunctional composite coating (HASiGdCe) by the plasma spraying technique. Notably, this is the first report of a HASiGdCe coating. After extensive experimental studies, we found that the HASiGdCe coating has the following four major advantages. First, the HASiGdCe coating has excellent microstructure, phase structure, wettability, bonding strength, corrosion resistance and bioactivity, which fully meet the standards for orthopedic implant coatings. In particular, for the bonding strength with the titanium substrate, the bonding strength of the HASiGdCe coating can be as high as 39.48 MPa, which is much higher than that of the HA coating (25.45 MPa) that has been used commercially. Second, with the ability to release Gd^{3+} and Ce^{4+}, the HASiGdCe coating showed significant antimicrobial effects against both gram-positive bacteria MRSA and gram-negative bacteria PAO-1. Third, the HASiGdCe coating exhibited excellent osteoinductivity both in vivo and in vitro due to the ingenious introduction of SiO2 NPs, Gd_2O_3 NPs, and CeO_2 NPs. Finally, as a result of the introduction of SiO_2NPs and CeO_2 NPs, the HASiGdCe coating has excellent angiogenic activity, which is vital for implantable biomaterials to achieve osseointegration. In conclusion, the HASiGdCe coating endows titanium implants with many excellent properties, which can effectively enhance the osseointegration of the implants while preventing bacterial infections and has broad application prospects in the treatment of bone defects caused by tumors, traumas, severe infections, osteoarthritis, osteoporosis, osteonecrosis, and other diseases. Despite the breakthrough of this study, there are still limitations that need to be further investigated. First, this study primarily explored the beneficial effects of HASiGdCe coatings over a relatively short timeframe. In the future, we will consider evaluating it over a longer time frame. Second, the antibacterial, osteogenic and vascularization effects of HASiGdCe coatings certainly involve many complex cellular and molecular mechanisms. It is necessary to explore these mechanisms and signaling pathways more deeply, which will be another of our future research directions.

Data Sharing Statement

The datasets used and/or analyzed during the current study are available from the corresponding author on reasonable request.

Ethics Approval and Consent to Participate

All animal experimental procedures were approved by the Animal Ethics Committee of Shandong University School of Stomatology (NO.20220614) and carried out in accordance with the UK Animals (Scientific Procedures) Act (1986).

Author Contributions

All authors made a significant contribution to the work reported, whether that is in the conception, study design, execution, acquisition of data, analysis, and interpretation, or all these areas; took part in drafting, revising or critically reviewing the article; gave final approval of the version to be published; have agreed on the journal to which the article has been submitted; and agree to be accountable for all aspects of the work.

Funding

This work was financially supported by the National Natural Science Foundation of China (NO. 81701008), National Natural Science Foundation of China (No. 51975338), Natural Science Foundation of Shandong Province, China (NO. ZR2023MH199), Special funds for Taishan Scholars Project of Shandong Province, China (NO. tsqn202306367), and Key research and development program of Shandong Province, China (NO. 2019GSF108187).

Disclosure

The authors report no conflicts of interest in this work.

References

1. Ke DX, Robertson SF, Dernell WS, Bandyopadhyay A, Bose S. Effects of MgO and SiO2 on plasma-sprayed hydroxyapatite coating: an in vivo study in rat distal femoral defects. *Acs Appl Mater Inter*. 2017;9(31):25731–25737. doi:10.1021/acsami.7b05574
2. Li X, Xu M, Geng Z, Liu Y. Functional hydrogels for the repair and regeneration of tissue defects. *Front Bioeng Biotechnol*. 2023;11:1190171. doi:10.3389/fbioe.2023.1190171
3. Xu L, Li JQ, Xu XJ, et al. A novel cytocompatibility strengthening strategy of ultrafine-grained pure titanium. *Acs Appl Mater Inter*. 2019;11(51):47680–47694. doi:10.1021/acsami.9b13554
4. Zhang JK, Zhou WH, Wang H, Lin KL, Chen FS. 3D-printed surface promoting osteogenic differentiation and angiogenetic factor expression of BMSCs on Ti6Al4V implants and early osseointegration in vivo. *J Mater Sci Technol*. 2019;35(2):336–343. doi:10.1016/j.jmst.2018.09.063
5. Zhou R, Han Y, Cao JY, et al. Enhanced osseointegration of hierarchically structured ti implant with electrically bioactive SnO2-TiO2 bilayered surface. *Acs Appl Mater Inter*. 2018;10(36):30191–30200. doi:10.1021/acsami.8b10928
6. Cao HL, Zhang WJ, Meng FH, et al. Osteogenesis catalyzed by titanium-supported silver nanoparticles. *Acs Appl Mater Inter*. 2017;9(6):5149–5157. doi:10.1021/acsami.6b15448
7. Zhang Y, Fu S, Yang L, Qin GW, Zhang E. A nano-structured TiO2/CuO/Cu2O coating on Ti-Cu alloy with dual function of antibacterial ability and osteogenic activity. *J Mater Sci Technol*. 2022;97:201–212. doi:10.1016/j.jmst.2021.04.056
8. Raphel J, Holodniy M, Goodman SB, Heilshorn SC. Multifunctional coatings to simultaneously promote osseointegration and prevent infection of orthopaedic implants. *Biomaterials*. 2016;84:301–314. doi:10.1016/j.biomaterials.2016.01.016
9. Geng Z, Li XP, Ji LL, et al. A novel snail-inspired bionic design of titanium with strontium-substituted hydroxyapatite coating for promoting osseointegration. *J Mater Sci Technol*. 2021;79:35–45. doi:10.1016/j.jmst.2020.11.041
10. Zhou H, Lee J. Nanoscale hydroxyapatite particles for bone tissue engineering. *Acta Biomater*. 2011;7(7):2769–2781. doi:10.1016/j.actbio.2011.03.019
11. Goodman SB, Yao ZY, Keeney M, Yang F. The future of biologic coatings for orthopaedic implants. *Biomaterials*. 2013;34(13):3174–3183. doi:10.1016/j.biomaterials.2013.01.074
12. Li M, Xiong P, Yan F, et al. An overview of graphene-based hydroxyapatite composites for orthopedic applications. *Bioact Mater*. 2018;3(1):1–18. doi:10.1016/j.bioactmat.2018.01.001
13. Cao L, Ullah I, Li N, et al. Plasma spray of biofunctional (Mg, Sr)-substituted hydroxyapatite coatings for titanium alloy implants. *J Mater Sci Technol*. 2019;35(5):719–726. doi:10.1016/j.jmst.2018.10.020
14. Sargin F, Erdogan G, Kanbur K, Turk A. Investigation of in vitro behavior of plasma sprayed Ti, TiO2 and HA coatings on PEEK. *Surf Coat Tech*. 2021;2021:411.
15. Roy M, Bandyopadhyay A, Bose S. Induction plasma sprayed nano hydroxyapatite coatings on titanium for orthopaedic and dental implants. *Surf Coat Tech*. 2011;205(8–9):2785–2792. doi:10.1016/j.surfcoat.2010.10.042
16. Turkoz M, Atilla AO, Evis Z. Silver and fluoride doped hydroxyapatites: investigation by microstructure, mechanical and antibacterial properties. *Ceram Int*. 2013;39(8):8925–8931. doi:10.1016/j.ceramint.2013.04.088
17. Bose S, Banerjee D, Robertson S, Vahabzadeh S. Enhanced in vivo bone and blood vessel formation by iron oxide and silica doped 3D printed tricalcium phosphate scaffolds. *Ann Biomed Eng*. 2018;46(9):1241–1253. doi:10.1007/s10439-018-2040-8
18. Gotz W, Tobiasch E, Witzleben S, Schulze M. Effects of silicon compounds on biomineralization, osteogenesis, and hard tissue formation. *Pharmaceutics*. 2019;11(3):117. doi:10.3390/pharmaceutics11030117
19. Hoppe A, Guldal NS, Boccaccini AR. A review of the biological response to ionic dissolution products from bioactive glasses and glass-ceramics. *Biomaterials*. 2011;32(11):2757–2774.

20. Li H, Chang J. Bioactive silicate materials stimulate angiogenesis in fibroblast and endothelial cell co-culture system through paracrine effect. *Acta Biomater*. 2013;9(6):6981–6991. doi:10.1016/j.actbio.2013.02.014
21. Shi MC, Xia LG, Chen ZT, et al. Europium-doped mesoporous silica nanosphere as an immune-modulating osteogenesis/angiogenesis agent. *Biomaterials*. 2017;144:176–187. doi:10.1016/j.biomaterials.2017.08.027
22. Aashima Pandey SK, Singh S, Mehta SK, Mehta SK. Biocompatible gadolinium oxide nanoparticles as efficient agent against pathogenic bacteria. *J Colloid Interf Sci*. 2018;529:496–504. doi:10.1016/j.jcis.2018.06.030
23. Keldani Z, Lord ML, McNeill FE, Chettle DR, Grafe JL. Coherent normalization for in vivo measurements of gadolinium in bone. *Physiol Meas*. 2017;38(10):1848–1858. doi:10.1088/1361-6579/aa87f0
24. Liao F, Peng XY, Yang F, Ke QF, Zhu ZH, Guo YP. Gadolinium-doped mesoporous calcium silicate/chitosan scaffolds enhanced bone regeneration ability. *Mat Sci Eng C*. 2019;2019:104.
25. Liu HF, Jin Y, Ge K, et al. Europium-doped Gd2O3 nanotubes increase bone mineral density in vivo and promote mineralization in vitro. *Acs Appl Mater Inter*. 2017;9(7):5784–5792. doi:10.1021/acsami.6b14682
26. Wei F, Neal CJ, Sakthivel TS, Kean T, Seal S, Coathup MJ. Multi-functional cerium oxide nanoparticles regulate inflammation and enhance osteogenesis. *Mat Sci Eng C*. 2021;2021:124.
27. Purohit SD, Singh H, Bhaskar R, et al. Gelatin-alginate-cerium oxide nanocomposite scaffold for bone regeneration. *Mater Sci Eng C*. 2020;2020:116.
28. Pop OL, Mesaros A, Vodnar DC, et al. Cerium Oxide nanoparticles and their efficient antibacterial application in vitro against gram-positive and gram-negative pathogens. *Nanomaterials*. 2020;10(8):1614. doi:10.3390/nano10081614
29. Zhang XY, Li FY, Li YL, et al. Comparison on multi-angle erosion behavior and mechanism of Cr3C2-NiCr coatings sprayed by SPS and HVOF. *Surf Coat Tech*. 2020;2020:403.
30. Zhao Z, Liu ML, Zhou QJ, Li MC. Hydrogen permeation behavior of QP1180 high strength steel in simulated coastal atmosphere. *J Mater Res Technol*. 2022;18:2320–2330. doi:10.1016/j.jmrt.2022.03.147
31. Campoccia D, Montanaro L, Arciola CR. The significance of infection related to orthopedic devices and issues of antibiotic resistance. *Biomaterials*. 2006;27(11):2331–2339. doi:10.1016/j.biomaterials.2005.11.044
32. Zeng XM, Xiong SJ, Zhuo SY, et al. Nanosilver/poly (DL-lactic-co-glycolic acid) on titanium implant surfaces for the enhancement of antibacterial properties and osteoinductivity (vol 14, pg 1849, 2019). *Int J Nanomed*. 2019;14:3469. doi:10.2147/IJN.S211778
33. Ebadi M, Buskaran K, Bullo S, Hussein MZ, Fakurazi S, Pastorin G. Synthesis and cytotoxicity study of magnetite nanoparticles coated with polyethylene glycol and sorafenib-zinc/aluminium layered double hydroxide. *Polymers-Basel*. 2020;12(11). doi:10.3390/polym12112716
34. Wang YL, Liang YY, Huang JC, et al. Proteomic analysis of silk fibroin reveals diverse biological function of different degumming processing from different origin. *Front Bioeng Biotech*. 2022;9. doi:10.3389/fbioe.2021.777320
35. Ding Y, Tao BL, Ma RC, Zhao X, Liu P, Cai KY. Surface modification of titanium implant for repairing/improving microenvironment of bone injury and promoting osseointegration. *J Mater Sci Technol*. 2023;143:1–11. doi:10.1016/j.jmst.2022.09.044
36. Tao BL, Yi WW, Qin X, et al. Improvement of antibacterial, anti-inflammatory, and osteogenic properties of OGP loaded Co-MOF coating on titanium implants for advanced osseointegration. *J Mater Sci Technol*. 2023;146:131–144. doi:10.1016/j.jmst.2022.11.013
37. Tao BL, Zhao WK, Lin CC, et al. Surface modification of titanium implants by ZIF-8@Levo/LBL coating for inhibition of bacterial-associated infection and enhancement of in vivo osseointegration. *Chem Eng J*. 2020;390:124621.
38. Wu SY, Shen XK, Chen MY, et al. Multifunctional TaCu-nanotubes coated titanium for enhanced bacteriostatic, angiogenic and osteogenic properties. *Mat Sci Eng C*. 2021;120:111777.
39. Liang SR, Li XS, Liu RJ, et al. Malvidin-3-O-glucoside ameliorates cadmium-mediated cell dysfunction in the estradiol generation of human granulosa cells. *Nutrients*. 2023;15(3):753. doi:10.3390/nu15030753
40. Yang JP, Shen CS, Zhu T, et al. An aminopeptidase N-based color-convertible fluorescent nano-probe for cancer diagnosis. *Biomater Sci*. 2023;11 (8):2809–2817. doi:10.1039/D3BM00007A
41. van Hengel IAJ, Tierolf MW, Valerio VPM, et al. Self-defending additively manufactured bone implants bearing silver and copper nanoparticles. *J Mater Chem B*. 2020;8(8):1589–1602. doi:10.1039/C9TB02434D
42. Wu ZJ, Shen J, Xu QM, et al. Epigallocatechin-3-gallate improves intestinal gut microbiota homeostasis and ameliorates clostridioides difficile infection. *Nutrients*. 2022;14(18):3756. doi:10.3390/nu14183756
43. Zhao XB, Peng C, You J. Plasma-Sprayed ZnO/TiO2 Coatings with Enhanced Biological Performance. *J Therm Spray Techn*. 2017;26 (6):1301–1307. doi:10.1007/s11666-017-0573-2
44. Zhang DW, Huang Y, Wang YC. Bonding performances of epoxy coatings reinforced by carbon nanotubes (CNTs) on mild steel substrate with different surface roughness. *Compos Part A*. 2021;147:106479.
45. Cotrut CM, Ionescu IC, Ungureanu E, et al. Evaluation of surface modification techniques on the ability of apatite formation and corrosion behavior in synthetic body fluid: an in vitro study. *Surf Interfaces*. 2021;22:100866.
46. Ren B, Wan Y, Wang GS, Liu ZQ, Huang Y, Wang HW. Morphologically modified surface with hierarchical micro-/nano-structures for enhanced bioactivity of titanium implants. *J Mater Sci*. 2018;53(18):12679–12691. doi:10.1007/s10853-018-2554-3
47. Ji YJ, Zhang HC, Ru JY, et al. Creating micro-submicro structure and grafting hydroxyl group on PEEK by femtosecond laser and hydroxylation to synergistically activate cellular response. *Mater Design*. 2021;199:109413.
48. Chen QY, Zou YL, Fu W, et al. Wear behavior of plasma sprayed hydroxyapatite bioceramic coating in simulated body fluid. *Ceram Int*. 2019;45 (4):4526–4534. doi:10.1016/j.ceramint.2018.11.137
49. Ke DX, Vu AA, Bandyopadhyay A, Bose S. Compositionally graded doped hydroxyapatite coating on titanium using laser and plasma spray deposition for bone implants. *Acta Biomater*. 2019;84:414–423. doi:10.1016/j.actbio.2018.11.041
50. Chen QY, Zou YL, Chen X, et al. Morphological, structural and mechanical characterization of cold sprayed hydroxyapatite coating. *Surf Coat Tech*. 2019;357:910–923. doi:10.1016/j.surfcoat.2018.10.056
51. Clavijo-Mejia GA, Hermann-Munoz JA, Rincon-Lopez JA, Ageorges H, Munoz-Saldana J. Bovine-derived hydroxyapatite coatings deposited by high-velocity oxygen-fuel and atmospheric plasma spray processes: a comparative study. *Surf Coat Tech*. 2020;381:125193.
52. Chambard M, Marsan O, Charvillat C, et al. Effect of the deposition route on the microstructure of plasma-sprayed hydroxyapatite coatings. *Surf Coat Tech*. 2019;371:68–77. doi:10.1016/j.surfcoat.2019.01.027

53. Xu HF, Geng X, Liu GX, et al. Deposition, nanostructure and phase composition of suspension plasma-sprayed hydroxyapatite coatings. *Ceram Int*. 2016;42(7):8684–8690. doi:10.1016/j.ceramint.2016.02.102
54. Ratha I, Datta P, Balla VK, Nandi SK, Kundu B. Effect of doping in hydroxyapatite as coating material on biomedical implants by plasma spraying method: a review. *Ceram Int*. 2021;47(4):4426–4445. doi:10.1016/j.ceramint.2020.10.112
55. Khor KA, Li H, Cheang P, Boey SY. In vitro behavior of HVOF sprayed calcium phosphate splats and coatings. *Biomaterials*. 2003;24(5):723–735. doi:10.1016/S0142-9612(02)00404-0
56. Tan L, Li J, Liu XM, et al. Rapid biofilm eradication on bone implants using red phosphorus and near-infrared light. *Adv Mater*. 2018;30 (31):1801808. doi:10.1002/adma.201801808
57. Li X, Xu X, Xu M, Geng Z, Ji P, Liu Y. Hydrogel systems for targeted cancer therapy. *Front Bioeng Biotechnol*. 2023;11:1140436. doi:10.3389/fbioe.2023.1140436
58. Xie K, Zhou ZA, Guo Y, et al. Long-term prevention of bacterial infection and enhanced osteoinductivity of a hybrid coating with selective silver toxicity. *Adv Healthc Mater*. 2019;8(5). doi:10.1002/adhm.201801465
59. Zhang KY, Lin SE, Feng Q, et al. Nanocomposite hydrogels stabilized by self-assembled multivalent bisphosphonate-magnesium nanoparticles mediate sustained release of magnesium ion and promote in-situ bone regeneration. *Acta Biomater*. 2017;64:389–400. doi:10.1016/j.actbio.2017.09.039
60. Gao P, Fan B, Yu XM, et al. Biofunctional magnesium coated Ti6Al4V scaffold enhances osteogenesis and angiogenesis in vitro and in vivo for orthopedic application. *Bioact Mater*. 2020;5(3):680–693. doi:10.1016/j.bioactmat.2020.04.019
61. Do Monte FA, Awad KR, Ahuja N, et al. Amorphous silicon oxynitrophosphide-coated implants boost angiogenic activity of endothelial cells. *Tissue Eng Pt A*. 2020;26(1–2):15–27. doi:10.1089/ten.tea.2019.0051
62. Nethi SK, Nanda HS, Steele TWJ, Patra CR. Functionalized nanoceria exhibit improved angiogenic properties. *J Mater Chem B*. 2017;5 (47):9371–9383. doi:10.1039/C7TB01957B